

# Atomic Layer Deposition-Derived Nanomaterials: Oxides, Transition Metal Dichalcogenides, and Metal–Organic Frameworks

Zhiwei Zhang,<sup>†</sup> Yuting Zhao,<sup>†</sup> Zhe Zhao, Gaoshan Huang, and Yongfeng Mei\*

Cite This: <https://dx.doi.org/10.1021/acs.chemmater.9b04414>

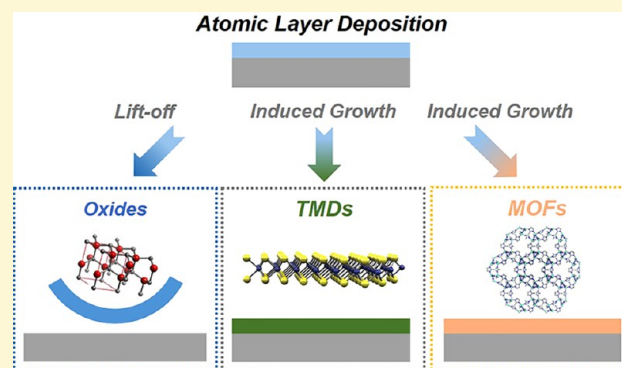
Read Online

ACCESS |

Metrics & More

Article Recommendations

**ABSTRACT:** Atomic layer deposition (ALD) is an effective technique of preparing nanomembranes with atomic scaling precision, high uniformity, superior conformality, and excellent accessibility on different substrates. Recently, some emerging methods have been derived to prepare nanomaterials that cannot be prepared directly by conventional ALD. For instance, ALD lift-off is an efficient method for preparing free-standing oxides nanostructures with precise size and controllable dimensions. The confinement from the substrate can thus be eliminated, and the corresponding device can be obtained via a micro/nano-fabrication process. ALD induced growth is a strategy of inducing chemical reactions on an ALD predeposited thin film through the post-treatment including vapor phase treatment or liquid phase treatment to prepare new materials and has been adopted in the synthesis of transition metal dichalcogenides and metal organic frameworks. In these perspectives, these ALD-derived technologies and newly developed materials can bring opportunities for the future advantageous applications. Here in this review we provide a comprehensive conclusion and understanding of these ALD-derived techniques and related promising nanomaterials.



## 1. INTRODUCTION

Nanomaterials have explored their applications in wide areas for their excellent performance, such as catalysis,<sup>1,2</sup> medicine,<sup>3</sup> sensors,<sup>4</sup> energy storage and conversion,<sup>5,6</sup> optoelectronics,<sup>7</sup> and many others. The performance of nanomaterials is closely related to the morphology, size, crystal surface, and composition.<sup>8</sup> Therefore, such a variety in tunable parameters provides huge engineering opportunities for the synthesis of nanomaterials.<sup>8,9</sup> Over the past decades, solution-based processes have been practiced for synthesizing nanomaterials including the hydrothermal method,<sup>10</sup> solution precipitation methods,<sup>11</sup> sol–gel methods,<sup>12</sup> and layer-by-layer (LBL) deposition.<sup>13,14</sup> These techniques, although being very promising, usually are not capable of precisely controlling uniformity, thickness, surface coverage, and morphology.<sup>8</sup> Atomic layer deposition (ALD), as a new versatile process for developing high quality nanomaterials, holds the capability of excellent thickness and composite controllability, unrivaled conformal coating, and good uniformity over a large scale.<sup>15–17</sup> It has obtained some advanced developments and promising achievements in various fields including microelectronics,<sup>18</sup> energy,<sup>19</sup> and biotechnology.<sup>20</sup>

ALD is a monolayer stepwise growth process that proceeds by exposing the substrate surface alternately to each precursor.<sup>15</sup> One typical ALD process consists of four steps: the pulse of precursor/purge/pulse of coreactant/purge. This

four-step process can be repeated to grow a desired material with precise control over the thickness.<sup>21</sup> By adjusting the duration of each exposure, all surface reactions go to completion and saturation before the next reaction starts, making the growth process self-limiting. The self-limiting nature of the half-reaction allows for conformal coatings on a complex three-dimensional (3D) surface, such as carbon nanotubes, polymers, or porous anodic aluminum oxide, making ALD a robust technique for developing various nanostructures.<sup>22,23</sup> Besides, by adopting the metal precursors with various counter-reactants, such as H<sub>2</sub>O, O<sub>2</sub>, O<sub>3</sub>, NH<sub>3</sub>, H<sub>2</sub>S, and H<sub>2</sub>, an enormous variety of materials including oxides, nitrides, sulfides, carbides, and elementary metals have been successfully produced.<sup>24,25</sup> It is noteworthy that the separated dosing of precursors ensures that no detrimental gas-phase reactions take place. The atomically controlled growth and the separated pulse of the reactant make it possible to apply multiple binary ALD processes into a super cycle for the

Received: October 28, 2019

Revised: October 7, 2020

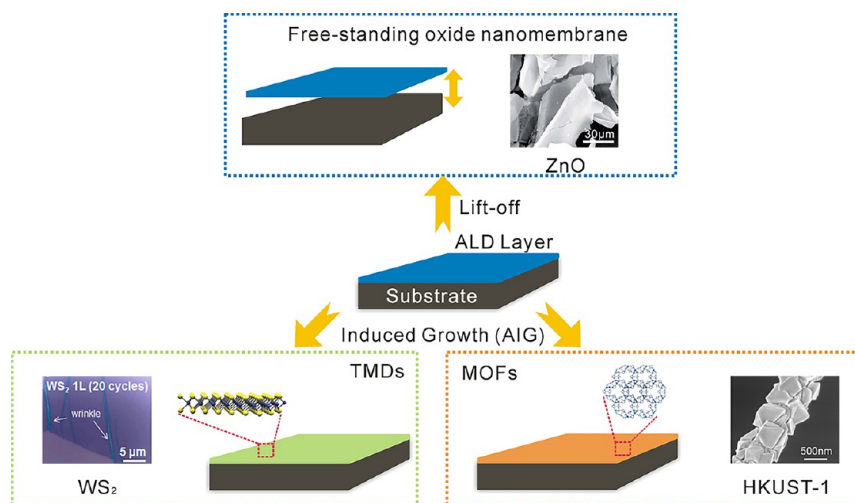


**Figure 1.** Schematic diagram illustrating ALD-derived nanomaterials: oxide nanomembranes by lift-off method, TMDs, and MOFs by AIG. The images in the insets are adapted with permission from ref 76 (Copyright Royal Society of Chemistry 2018), ref 107 (Copyright American Chemical Society 2013), and ref 147 (Copyright American Chemical Society 2015).

creation of multicomponent nanomaterials.<sup>26</sup> This versatility allows for a wealth of doped, well-mixed, or nanolaminate ternary/quaternary materials with composition variation at the atomic level.<sup>27–33</sup>

It is noted that the advantage of ALD originally was to prepare dense and uniform films.<sup>21–23</sup> These products mainly include metal oxides, nitrides, and some elemental metal films.<sup>25,34–36</sup> Here we use term “nanomembrane” to define these films when the thickness of the films is in the range of one to a few hundred nanometers.<sup>37</sup> Because of their dimensionality, the nanomembranes may have properties different from those of the bulk. They are lightweight and flexible and show a large exposed surface and significant quantum confinement effect.<sup>38,39</sup> Therefore, the nanomembranes can be distributed over a large surface area, deformed into various shapes, and wrapped onto a curvilinear surface, leading to a broad spectrum of applications in catalyst, sensing, biomedicine, and energy harvesting.<sup>40–45</sup> The nanomembranes prepared by ALD are normally supported by the bulk substrates; this attachment may disturb these properties.<sup>37</sup> The lift-off ALD method has demonstrated its viability to prepare free-standing nanostructures by releasing the deposited nanomembrane from the sacrificial substrate or selectively removing the template, while oxide nanostructures are the objects of much research. Some typical examples such as free-standing  $\text{TiO}_2$  nanomembranes and ZnO nanosheets have been successfully fabricated and adapted to some devices (a typical example of ZnO with atomic structures was exhibited in Figure 1).<sup>46,47</sup> The lift-off ALD method accesses a wide material set with well-controlled thickness and composition. Therefore, a particular summary on the methods, materials, and application of ALD for free-standing oxide nanostructures has been recorded here. It can be predicted that such methods may be popularized for preparing other free-standing nanostructures made from, e.g., nitrides and metals, and giving full play to their properties.

Notably, some breakthroughs have recently been made in the ALD for transition metal dichalcogenides (TMDs) and metal–organic frameworks (MOFs), which are as two “star” materials in the electronic and energy domains (Figure 1). These materials are typically prepared by chemical vapor

deposition (for TMDs),<sup>48</sup> epitaxial growth (for TMDs),<sup>49</sup> and hydrothermal methods (for MOFs),<sup>50</sup> which means that ALD techniques are not on the list of commonly used preparation methods for these materials. However, in some cases, these traditional methods have certain limitations and disadvantages. For the TMD materials, the reduction gases such as hydrogen are commonly required by CVD to facilitate the reduction of halogen species, which is not conducive to the waste gas treatment, and the whole process is complex. Besides, some metal or metal oxide precursors with high melting points are difficult to vaporize and react with gaseous chalcogen precursors during the CVD process.<sup>48</sup> Moreover, it is still challenging to fabricate TMD materials through the fast synthesis route with a large domain size.<sup>49</sup> For MOFs, the solvothermal method usually needs to be carried out in an autoclave. For instance, for two typical MOF materials, HKUST-1<sup>51</sup> and UiO-66,<sup>52</sup> both of them need to be synthesized in organic solvents at a temperature higher than 100 °C for a long time. This obviously makes the reaction more difficult and dangerous. It is also difficult to control the crystallization and the morphology during the reaction.<sup>50</sup>

In order to address these challenges, a strategy based on the post-treatment of the ALD preinduced materials has been developed to assemble these materials, which shows a promising universality. This ALD-induced growth (AIG) consists of the preparation of induced layers or guide layers by ALD and the subsequent modified synthesis of a specific product through the liquid or vapor phase post-treatment. It can also be seen as an innovative bottom-up deposition method related to ALD. Since the ALD can synthesize a film with a large size, this approach is also capable of fabricating TMD films and MOF films with large areas. For TMDs, the induced layers are normally metal or metal oxide films, and there is no need to consider the melting point problem.<sup>53</sup> For MOFs, this strategy could be implemented in the liquid or gas phases and sometimes requires lower temperatures.<sup>54,55</sup> The AIG method has been utilized to prepare some layered materials that were difficult to synthesize directly by ALD and otherwise required complex processes.<sup>56</sup> Besides, inheriting from the ALD technology, AIG has the advantages of controllable scale, a steerable reaction process, and diversified

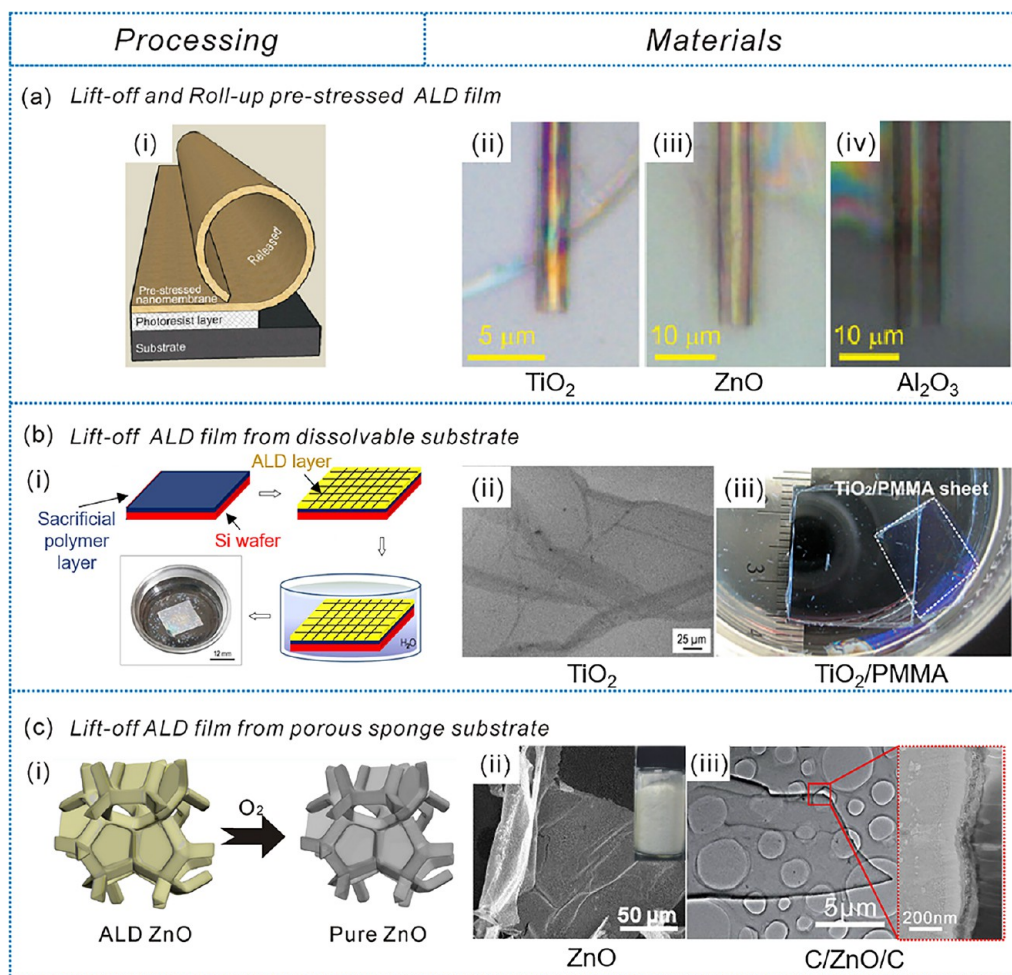


**Figure 2.** Fabrication of free-standing nanomembranes. (a) Lift-off and rolling of a prestressed nanomembrane. (i) Schematic diagram illustrating the process to release and shape a prestressed nanomembrane into a tube on a photoresist. (ii–iv) Optical images of rolled-up TiO<sub>2</sub>, ZnO, and Al<sub>2</sub>O<sub>3</sub> nanomembranes. Adapted with permission from ref 68. Copyright 2008 Wiley-VCH Verlag. (b) Lift-off ALD nanomembrane from a dissolvable sacrificial layer. (i) Schematic diagram illustrating the fabrication process. (ii) SEM images of TiO<sub>2</sub> nanomembranes with 100 ALD cycles. Adapted with permission from ref 69. Copyright 2016 Elsevier BV. (iii) Pictures of TiO<sub>2</sub>/PMMA bilayer sheets. Adapted with permission from ref 46. Copyright 2014 American Chemical Society. (c) Lift-off ALD nanomembrane from the porous sponge substrate. (i) Schematic illustration of the fabrication process of ZnO nanomembranes by ALD onto a porous sponge substrate. (ii) SEM image of the ZnO nanomembrane. Inset is the digital photo of a bottle of free-standing ZnO nanomembranes. Reprinted with permission from ref 74. Copyright 2018 Royal Society of Chemistry. (iii) SEM image of C/ZnO/C nanomembranes. The cross-sectional image and the elemental distributions are also demonstrated. Adapted with permission from ref 76. Copyright 2018 Royal Society of Chemistry.

deposition substrates.<sup>56</sup> The advantages offered by the AIG could promote the development of these materials and provide more creativity, in, e.g., flexible electronics, stretchable energy generating devices, and micronano-robotics.

Particularly, AIG can be divided into AIG-vapor and AIG-liquid, two paths according to different postprocessing models. Different scopes and features can be obviously seen from the two routes. So far, the utilization of AIG has made progress in the controlled synthesis of some materials, in which the TMDs and MOFs are two typical representatives. Some achievements and reviews<sup>57,58</sup> have been made on these materials while few comprehensive conclusions and insights on this AIG strategy have been made, such as the types of materials that can be synthesized and similarities, differences, superiorities, and weaknesses on this topic.

Here in this review, we provide a comprehensive understanding of ALD-derived materials including free-standing oxide nanomembranes and TMD and MOF films, which are discussed in Sections 2, 3, and 4, respectively. In the final

section, some general conclusions are made and some novel applications are proposed for these ALD-derived materials.

## 2. OXIDES

### 2.1. Free-Standing Oxide Nanomembranes.

Free-standing nanomembranes with two-dimensional layer structure have recently attracted ever-growing attention. Their dimensionality can drastically alter their physical, chemical, and optical properties as compared to their counterparts in other dimensions, which provides them with great potential as a flexible thin-film transistor, in optoelectronics, as an energy storage device, and in biomedical applications.<sup>59–64</sup> The lift-off ALD method has been demonstrated as a viable means to prepare free-standing nanomembrane materials. The free-standing nanomembranes are achieved by depositing an inorganic film onto a polymer sacrificial substrate and subsequently removing the substrate by physical dissolving/chemical etching methods. The solvent used is able to dissolve/etch the sacrificial layer over almost any inorganic

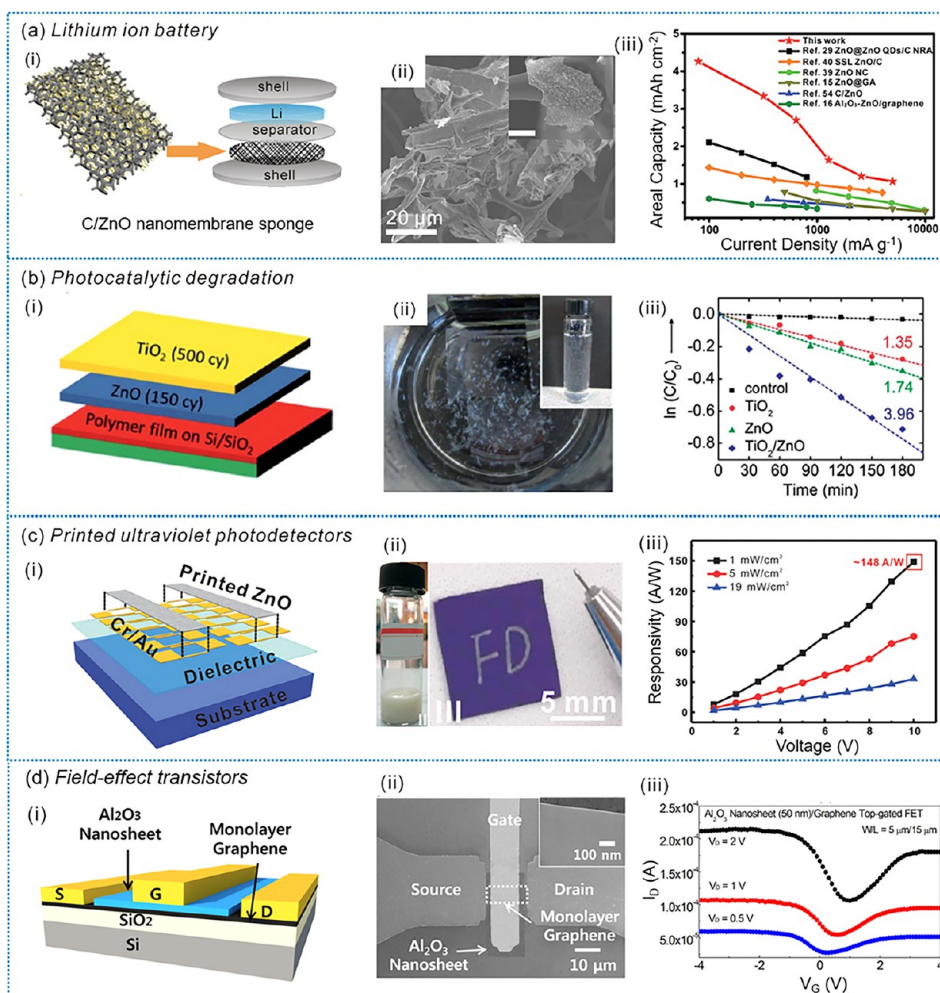


**Figure 3.** (a) C/ZnO nanomembrane sponge and its performance in lithium storage. (i) Schematic diagram and (ii) SEM image of the C/ZnO nanomembrane sponge. (iii) Areal capacity of the C/ZnO nanomembrane sponge anode for the Li-ion battery and other ZnO-based anodes. Adapted with permission from ref 74. Copyright 2018 Royal Society of Chemistry. (b) ZnO/TiO<sub>2</sub> bilayer nanomembranes and their performances in photocatalytic degradation. (i) Schematic illustration of the fabrication process of ZnO/TiO<sub>2</sub> by performing 150 cycles of ZnO and 200 cycles of TiO<sub>2</sub>. (ii) Picture of TiO<sub>2</sub>/ZnO bilayer nanomembranes dispersed in DI water and nanomembranes collected in a vial (inset). (iii) Photodegradation of methyl orange with UV-irradiation time with no nanomembranes, TiO<sub>2</sub> nanomembranes, ZnO nanomembranes, and ZnO/TiO<sub>2</sub> bilayer nanomembranes. Adapted with permission from ref 73. Copyright IOP Science 2014. (c) ZnO nanomembrane based printed ultraviolet photodetector and performance. (i) Schematic illustration of a printed ZnO nanomembrane based ultraviolet photodetector. (ii) Photo of the ZnO nanomembrane-based nanoink and letters “FD” on the silicon oxide substrate written by using the nanoink. (iii) Responsivity of the ultraviolet photodetector under different irradiated power densities. Adapted with permission from ref 78. Copyright 2019 American Institute of Physics. (d) Application of the free-standing Al<sub>2</sub>O<sub>3</sub> nanomembrane in fabricating the FET device. (i) Schematic and (ii) SEM image of the top-gated graphene FET device. Inset in panel (ii): SEM image with large magnification showing the 50 nm Al<sub>2</sub>O<sub>3</sub> nanomembrane on graphene. (iii) Transfer curve of the FET. Reprinted with permission from ref 81. Copyright American Chemical Society 2014.

material with practically 100% selectivity.<sup>37</sup> Therefore, many material sets could be engaged in fabricating free-standing nanomembranes. More importantly, shaping nanomembranes into three-dimensional architectures like rolled-up tubes can provide fascinating applications in photonics, medicines, fluidics, and biosensors.<sup>65–67</sup>

Mei et al.<sup>68</sup> developed a versatile method to roll a prestressed ALD nanomembrane with a simultaneous releasing process (Panel (i) of Figure 2a). The strain and strain gradient were introduced during deposition by heating or cooling the materials with different coefficients of thermal expansion. For the ALD Al<sub>2</sub>O<sub>3</sub> nanomembrane, the researchers kept the substrate temperature at 80 °C for the bottom layer and room temperature for the top layer.<sup>68</sup> This process exerted good and predictable control over the strain state during film deposition.

After dissolving the sacrificial layer (here: photoresist) by acetone, the film was released and rolled up into the micronanostructure. TiO<sub>2</sub>, ZnO, and Al<sub>2</sub>O<sub>3</sub> microtubes were obtained as shown in Panels (ii), (iii), and (iv) of Figure 2a. Because the photoresist layer could be patterned using conventional photolithography, the above nanomembrane was self-patterned during deposition,<sup>68</sup> thus providing convenience in accurate positioning of the rolled-up nanomembrane and modeling integration on a single chip.

Lee et al.<sup>46</sup> and Edy et al.<sup>69</sup> utilized dissolvable poly(vinyl alcohol) (PVA) and poly(acrylic acid) (PAA) as the sacrificial layer (Figure 2b) to synthesize free-standing oxide nanomembrane materials. They chose PVA and PAA as the sacrificial layers because of their ability to promote ALD metal oxide nucleation and their water solubility.<sup>46</sup> The TiO<sub>2</sub>

nanomembrane with controlled thickness was first deposited onto sacrificial layer and then was released and floated on the surface of water by dissolving PVA in deionized water (Panel (i) of Figure 2b).<sup>69</sup> The synthesized nanomembrane was uniform and showed ultrathin and flexible properties (Panel (ii) of Figure 2b).<sup>69</sup> By simply changing ALD cycles, the thickness of the TiO<sub>2</sub> nanomembrane was precisely tuned. Free-standing ZnO nanomembranes and Al<sub>2</sub>O<sub>3</sub> nanomembranes were also synthesized by using this method. The thinnest thickness that could be isolated and imaged was 1.1 nm and 1.3 nm for Al<sub>2</sub>O<sub>3</sub> and TiO<sub>2</sub> nanomembranes.<sup>41</sup> The sacrificial layer showed the effect on the resulting nanomembrane thickness, lateral size, and surface structure. From Lee's report, PVA was the most suitable substrate to separate the ALD film with the larger size (up to 5 mm across) while the PAA polymer led to small pieces less than 1 μm across.<sup>46</sup> This was because PAA showed high solubility and dissolved faster in water. The rapid dissolution likely added stress to the adhering ALD layer, causing a break and fracture of the oxide layer. The ALD lift-off method could also be used to create organic/inorganic bilayer heterojunction nanomembranes. For example, Lee et al.<sup>46</sup> utilized the PMMA/PVA bilayer polymer stack to obtain the oxide/PMMA bilayer sheet (Panel (iii) of Figure 2b). Because PMMA dissolved in a different solution from PVA, after dissolving PVA in water, free-standing TiO<sub>2</sub>/PMMA and ZnO/PMMA sheets were obtained. The synthesized organic/inorganic bilayers had separated organic and inorganic regions which may endow them unique characters for applications in the fields of electronics, optics, and bioengineering.<sup>70–72</sup>

However, only a small amount of the oxide layer was deposited on the substrate arising from the limited available surface area of the planar substrate.<sup>46,69</sup> By using ALD ZnO on porous sponge template with a larger surface, Pan et al.<sup>73</sup> synthesized large amounts of TiO<sub>2</sub> nanomembranes (Figure 2c). Facilitated by the intrinsic advantage of ALD technology, the deposited TiO<sub>2</sub> film conformally coated on all "skeletons" of the sponge.<sup>73</sup> After thermal removal of the template, a monolithic TiO<sub>2</sub> sponge was obtained with the microstructure duplicating the original template (Panel (i) of Figure 2c). Numerous nanomembranes were obtained after ultrasonic treatment of the TiO<sub>2</sub> sponge in solution. Zhao et al.<sup>74</sup> also obtained ZnO nanomembranes by using the sponge-templated ALD process (Panel (ii) of Figure 2c). By changing the thermal-treatment temperature, TiO<sub>2</sub> nanomembranes with anatase and mixed anatase and rutile phases were obtained. Besides the single phase nanomembrane, ALD is feasible for designing multiple-compound-layered structures by applying a multiple binary ALD process into a supercycle.<sup>26</sup> As an example, TiO<sub>2</sub>-ZnO composite nanomembranes were synthesized by performing *m* cycles of the TiO<sub>2</sub> binary process and *n* cycles of the ZnO binary process.<sup>75</sup> The tuning of the composition was achieved by changing the *m/n* ratio, the deposition sequence, and the arrangement of the sublayer stacks. Besides, by pyrolyzing the ZnO layer coated sponge template in inert gas, a sandwiched structure, porous carbon/metal oxides/porous carbon nanomembranes, was obtained (Panel (iii) of Figure 2c).<sup>76</sup> During the pyrolysis process, the template was transferred to carbon. Meanwhile, hydrocarbons generated with increasing temperature underwent a secondary pyrolytic deposition on all exposed surfaces. As in the case of porous carbon/ZnO/porous carbon (C/ZnO/C) nanomembranes with 200 ALD cycles of ZnO, the nanomembranes

consisted of a three-layer structure with 32 nm ZnO sandwiched between two carbon layers with thicknesses of 30 and 38 nm, respectively (Panel (iii) of Figure 2c).

These synthesized nanomembranes with favorable thickness, crystalline phase, and composition showed the desired performance as a supercapacitor,<sup>77</sup> in printed electronics,<sup>78</sup> as a lithium ion battery,<sup>74,79,80</sup> and as a photocatalyst.<sup>46,69,73,75</sup> ZnO nanomembranes demonstrated their superiority for fast and long-lifespan lithium storage by providing a shortened ion diffusion length and accommodating strain.<sup>76,79</sup> When uniformly dispersing ZnO nanomembranes in a carbon foam matrix, ZnO nanomembranes adhered to the carbon foam framework closely (Panels (i) and (ii) of Figure 3a).<sup>74</sup> The synthesized anode retained 92% capacity after 700 cycles at 2 A g<sup>-1</sup> and after 500 cycles at 5 A g<sup>-1</sup>. The large surface area and high porosity of the carbon foam also increased the mass loading of ZnO nanomembranes. Thus, the composite C/ZnO nanomembranes foam manifested a remarkable areal capacity of 4.3 mAh g<sup>-1</sup> (Panel (iii) of Figure 3a). On the other hand, the C/ZnO/C nanomembranes showed great promise for fast and stable lithium ion storage.<sup>76</sup> The capacity was up to 330 mAh g<sup>-1</sup> at 5000 mA g<sup>-1</sup>, and no obvious capacity decay was observed after 1650 cycles. The fast and stable charge/discharge performance was because the outer thick carbon coating enhanced conductivity and suppressed the expansion of the inner oxides. The performance of the composite nanomembrane showed significant dependence on the thickness and composition. The authors investigated the stability of the solid-electrolyte interphase of CZC nanomembranes with different ZnO layer thicknesses.<sup>76</sup> The study pointed out that a critical thickness ratio of ZnO to the carbon layer may exist, and the carbon layer was prone to fracture in the case of a large thickness ratio. The results have important applications in designing carbon/metal oxide composites for high performance anodes of Li-ion batteries. Li et al.<sup>79</sup> have also synthesized the ZnO nanomembrane onto expanded graphite and got a self-standing paper-like film. The expanded graphite provided mechanical support for ZnO, which avoided the pulverization of ZnO. Therefore, the composite shows a high stable capacity of 438 mAh g<sup>-1</sup> after charging and discharging for 500 cycles.

TiO<sub>2</sub> nanomembranes have especially drawn much attention in photocatalytic systems because of larger contact area between the TiO<sub>2</sub> nanomembrane and the solution and the thinner carrier diffusion length. Pan et al.<sup>73</sup> investigated the crystalline phase effect on the photocatalytic degradation performance of TiO<sub>2</sub> nanomembranes. They found that the TiO<sub>2</sub> nanomembrane with mixed anatase and rutile phase showed better photocatalytic performance than the pure anatase TiO<sub>2</sub> nanomembrane. This was ascribed to the synergy between anatase and rutile which led to spatial charge separation and hindered the recombination.<sup>73</sup> In addition, the TiO<sub>2</sub>/ZnO bilayer structure showed an enhanced photocatalytic rate compared with the single compound TiO<sub>2</sub> nanomembrane and ZnO nanomembrane (Panels (i), (ii), and (iii) of Figure 3b).<sup>47</sup> The increase was ascribed to the separation of photogenerated electrons and holes and spatially separated oxidation and reductions to different sides of the nanomembrane.<sup>42</sup> Printing electronic technology has some advantages over the traditional device fabrication technology with regard to simple fabrication, large-area production, and low cost. Guo et al.<sup>78</sup> used ZnO nanomembranes as the electrical constitution of nanoinks to prepare printed ultraviolet photodetectors (Panels (i) and (ii) of Figure 3c). The

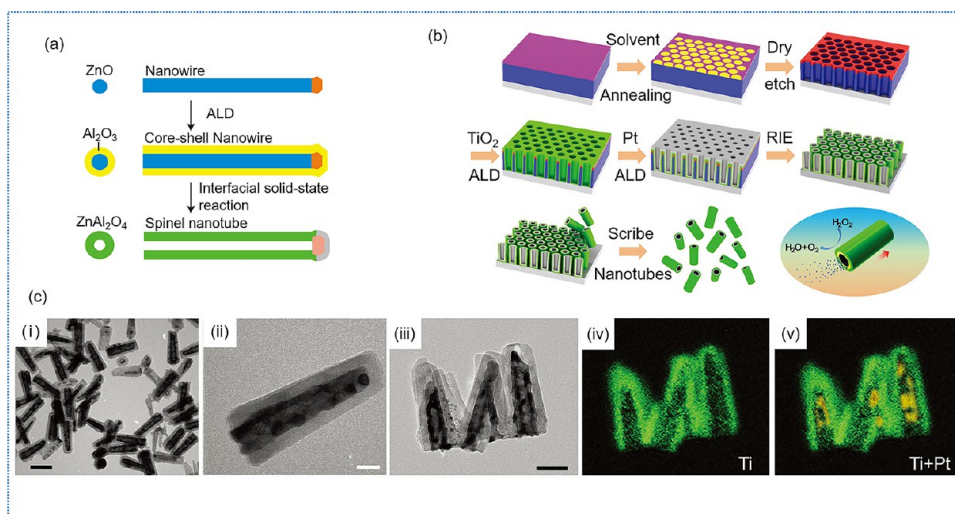


**Figure 4.** (a) Schematic illustration of the transformation of ZnO/Al<sub>2</sub>O<sub>3</sub> core-shell nanowires to ZnAl<sub>2</sub>O<sub>4</sub> nanotubes by means of the Kirkendall effect. Adapted with permission from ref 92. Copyright Springer Nature 2006. (b) Schematic of nanoconfined ALD of TiO<sub>2</sub>/Pt nanorockets. Adapted with permission from ref 95. Copyright Wiley 2017. (c) Characterization of nanorockets. TEM images of (i) a group of TiO<sub>2</sub>/Pt nanorockets and (ii) a zoom-in single nanorocket, showing the mildly conical structure of the nanorocket. (iii) TEM image and STEM-EELS elemental maps of (iv) Ti and (v) Ti + Pt. Scale bars: (i) 100 nm; (ii) 20 nm; (iii–v) 50 nm. Adapted with permission from ref 95. Copyright Wiley 2017.

printed film from the two-dimensional (2D) nanomembrane based nanoink reduced the grain boundaries and enabled a full surface coverage, leading to high-performance electronic thin films. Such a printed ultraviolet photodetector exhibited a high responsivity of 148 A/W (Panel (iii) of Figure 3c) and a response time of 19 s. This study provided a practical method to produce large amounts of functional nanomembranes for printing electronics and paved the way for developing high-performance, low cost, and large-area printing or flexible electronics. The same method can also be used to produce some key components of microelectronic devices. Kim and colleagues<sup>81</sup> carried out ALD on a sacrificial layer to fabricate transferrable free-standing Al<sub>2</sub>O<sub>3</sub> nanomembranes and successfully applied them into field-effect transistors (FET) as a high-*k* dielectric material (Figure 3d). As the schematic (Panel (i) of Figure 3d) and the SEM image (Panel (ii) of Figure 3d) show, the Al<sub>2</sub>O<sub>3</sub> nanomembrane was transferred onto the graphene matrix utilized as a gate dielectric. Panel (iii) of Figure 3d shows  $I_D$ – $V_G$  curves with different  $V_D$  values, and the results indicate that the increase in  $V_D$  induces the increased current and the shift of the curves to the positive voltage direction. It can be calculated that the field-effect mobilities are  $\sim 2200$  and  $\sim 800$  cm<sup>2</sup>/(V s) for the hole and electron, respectively. This typical work demonstrates that the ALD-derived transferrable nanomembranes can be used for the assembly of microelectronic devices. This also provides a feasible route for mass production of high-performance flexible electronic devices.<sup>81</sup>

**2.2. Free-Standing Oxide Nanopillars and Nanotubes.** ALD technology combined with the template-assisted method is capable of preparing three-dimensional complex nanostructures like nanopillars and nanotubes.<sup>82–87</sup> This approach has been reviewed in several excellent works.<sup>16,23,24,88</sup> Particularly, Hu et al.<sup>88</sup> have systematically reviewed the relevant materials and technologies involved in this approach and given comprehensive conclusions. Therefore, here we briefly introduce some advanced free-standing nanotube and nanopillar structures derived from the ALD technique.

The template-based ALD approach has been extensively investigated in the synthesis of nanotubes by using a two-step growth process: the deposition of the target material on a nanostructured template and the subsequent removal of the template via high temperature thermal treatment or chemical etching to obtain the free-standing nanostructure.<sup>16,23,24,89</sup> Mainly three types of templates including a CNT,<sup>21,82–84</sup> anodic aluminum oxide (AAO),<sup>90,91</sup> and polymeric templates (polymer nanofiber)<sup>85–87</sup> have been used. These structures possess a well-defined nanoscale tubular geometry, which could be functionalized or used as a template for nanotubes of various inorganic materials. As an example, Min et al.<sup>83</sup> first reported the fabrication of RuO<sub>2</sub> nanotubes via ALD on CNT arrays by using Ru(od)<sub>3</sub>/*n*-butylacetate solution (od = octane-2,4-dionate) and O<sub>2</sub> as precursors at 300 °C. The resultant Ru-coated CNT arrays were then oxidized at 500 °C in O<sub>2</sub> to remove the inner CNTs, resulting in free-standing RuO<sub>2</sub> nanotubes. Jin Fan et al.<sup>92</sup> first reported the fabrication of single-crystal ZnAl<sub>2</sub>O<sub>4</sub> spinel nanotubes by the Kirkendall-based fabrication route as shown in Figure 4a. A uniform amorphous Al<sub>2</sub>O<sub>3</sub> layer was deposited on the single crystal ZnO nanowire (diameter: 10–30 nm, length: up to 20 μm) by ALD to form the ZnO/Al<sub>2</sub>O<sub>3</sub> core-shell nanowires. The interfacial solid-state reaction and diffusion occurred when the nanowire was annealed in air at 700 °C. In this case, a complete ZnAl<sub>2</sub>O<sub>4</sub> spinel nanotube was formed by an extreme Kirkendall process, where only one-way migration of ZnO into Al<sub>2</sub>O<sub>3</sub> occurred.<sup>92</sup> In another spinel system such as MgAl<sub>2</sub>O<sub>4</sub>, the formation of the tubular structure was not directly due to the Kirkendall effect.<sup>93</sup> MgO nanowires were coated with a conformal Al<sub>2</sub>O<sub>3</sub> layer by ALD and were subsequently annealed at 700 °C to activate the interfacial reaction. The diffusion involved counter-diffusion of Mg<sup>2+</sup> and Al<sup>3+</sup> cation pairs while the oxygen sublattice was fixed, known as the Wagner counterdiffusion mechanism. Because of excess of MgO core for the complete spinel reaction, part of the core MgO nanowire remained to form the MgAl<sub>2</sub>O<sub>4</sub>–MgO shell-core coaxial nanowire. By selective removal of the MgO core in

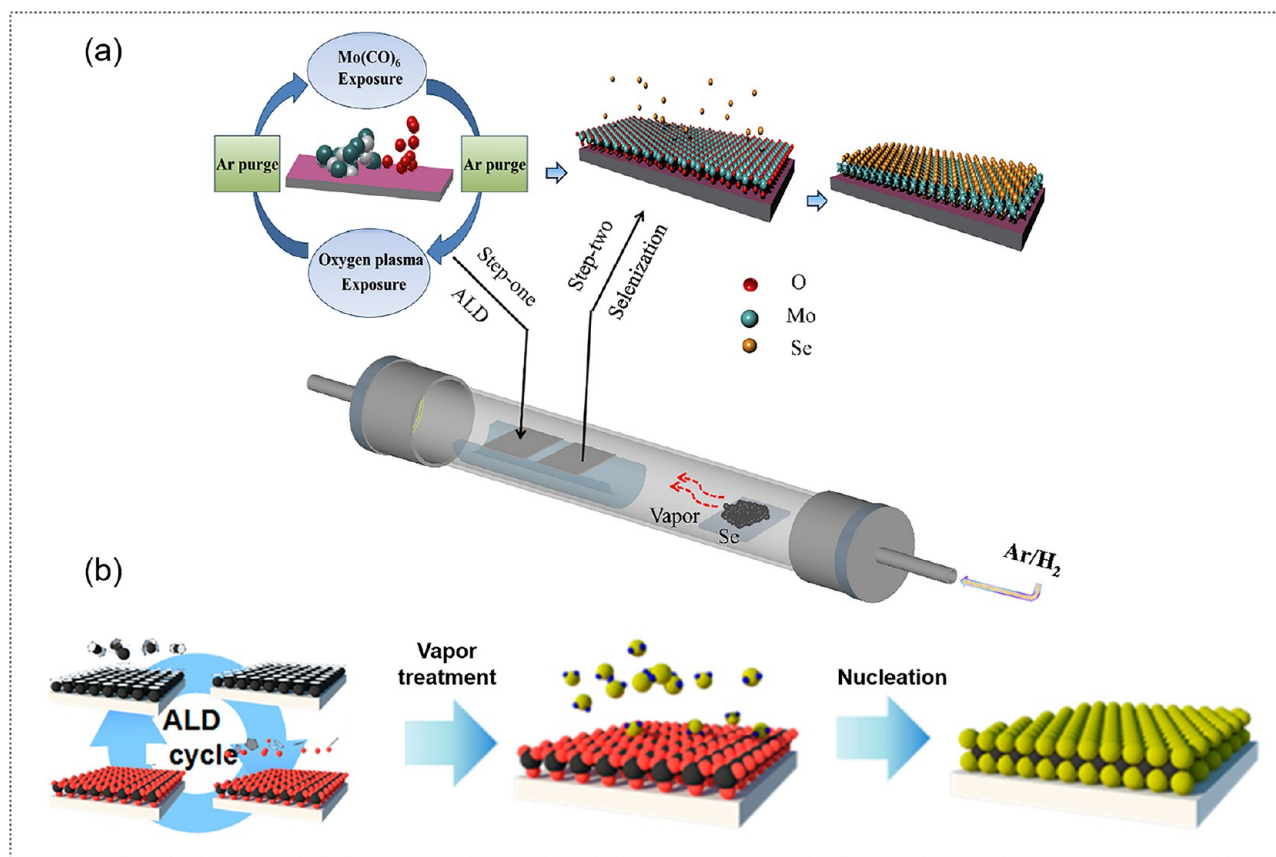


**Figure 5.** (a) Schematic of the ALD process of MoSe<sub>2</sub> nanosheets. Reprinted with permission from ref 106. Copyright Springer 2018. (b) Schematic of the TMD growth based on the ALD strategy. Adapted with permission from ref 107. Copyright American Chemical Society 2013.

aqueous (NH<sub>3</sub>)<sub>2</sub>SO<sub>4</sub> solution, the single-phase spinel nanotubes were obtained. This process can also be extended to form other MgO-based spinel oxide nanotubes by coating MgO nanowires with other ALD-processable oxides.<sup>93</sup>

The lithography technique has also been used to produce a highly periodic and ordered nanostructure as the template for the ALD synthesis of the nonplanar nanostructure. By combining the ALD with the block copolymer lithography, highly ordered free-standing TiO<sub>2</sub> nanopillar arrays with atomic layer control of the wall thickness were fabricated.<sup>94</sup> Similarly, Li et al.<sup>95</sup> reported the smallest man-made rocket engine, i.e., TiO<sub>2</sub>/Pt nanotubes (Figure 4b,c). In the experiment, the vertically cylindrical nanopore array with a length of 150 nm and diameter of 60 nm was fabricated by block copolymer lithography. Then the subsequent depositions of the TiO<sub>2</sub> and Pt layers were carried out by ALD. After removal of the overlayers and outer template by reactive ion etching and calcining, the freestanding coaxial TiO<sub>2</sub>/Pt nanotubes containing a hollow cylindrical chamber with an inner diameter down to 20 nm were obtained.<sup>95</sup>

It is obvious to see that one of the advantages of the ALD-derived free-standing oxide nanostructures is that the combination of ALD and micro/nano-fabrication technology enables the fabrication of complex nanostructures that are detached from the substrate by a relatively simple approach. These interesting structures greatly broaden the application of ALD technology in various fields, which are not only the preparation of nanoscale materials with controllable thickness but also the fabrication/assembly of various novel devices, such

as tubular optical microcavities, electrodes, and transistors.<sup>68,74,78,81</sup>

### 3. TMDs

In parallel to the intensive research on graphene-like materials, TMDs and MX<sub>2</sub> (M = Mo or W and X = S, Se, or Te) have attracted wide attention owing to their excellent electrical and optical properties.<sup>96–98</sup> Growth of layered MX<sub>2</sub> onto a support requires controlling the deposition at the atomic scale. Because of its relative low temperature, reproducibility, versatility, and layer-controlled precision of the thickness, ALD appears to be an excellent technique to synthesize 2D materials.<sup>99</sup>

For the preparation of TMD materials directly by ALD, some reports and reviews have been published,<sup>100–104</sup> which have made some systematic conclusions on the precursors, materials types, and characterizations. However, due to the limitation of the organic precursors of ALD, the complexity of the whole process (such as the equipment construction and exhaust gas treatment) and the high cost (normally the precursors), a facile strategy based on the first-step ALD and second-step thermal treatment has become an attractive way to fabricate controllable TMDs layers.<sup>56</sup> Besides, the post-treatment of the chemical vapor reaction to form target materials is also an effective and cheap method to synthesize TMDs which has been emphasized by Manzeli et al.<sup>105</sup> For example, Dai and colleagues implement ALD and the following vapor treatment to produce the MoSe<sub>2</sub> films through the selenization of an induced layer of ALD MoO<sub>3</sub> in the furnace tube as displayed in Figure 5a.<sup>106</sup> This method is essentially performed using the nucleation reaction of the induced/

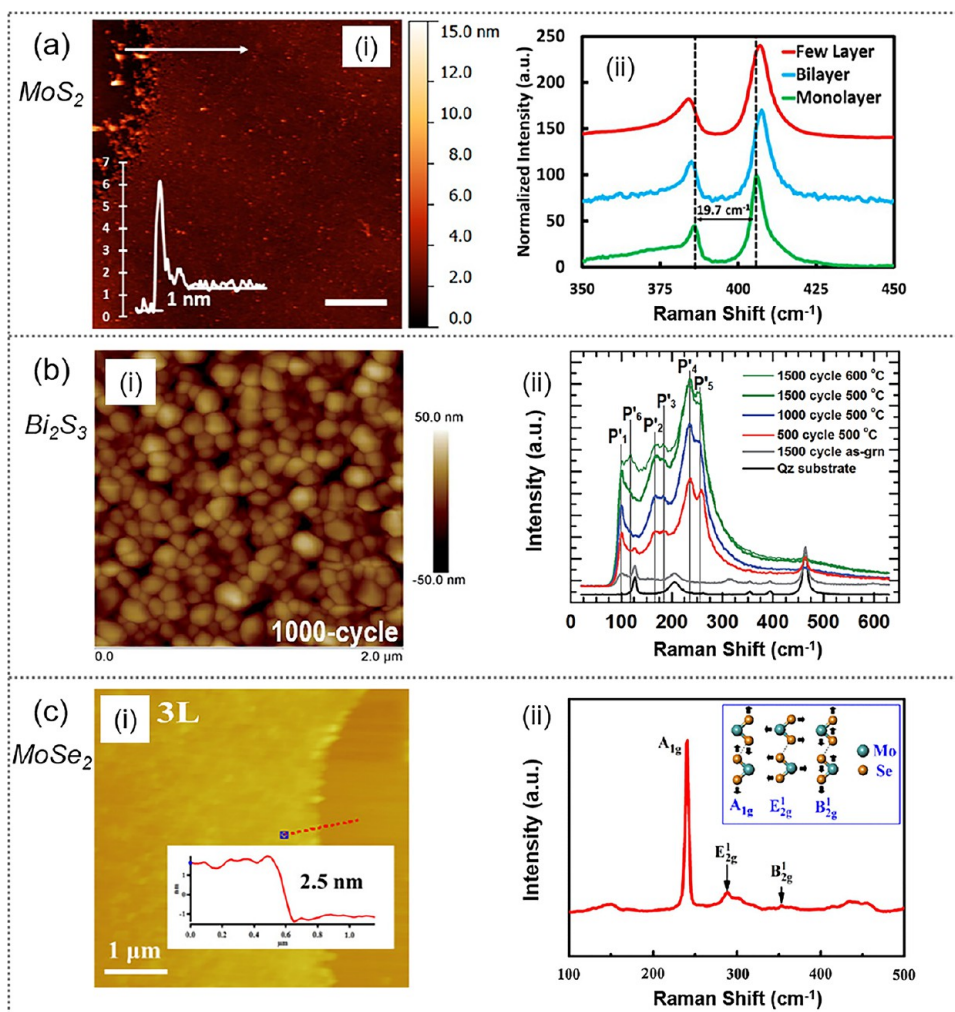


**Figure 6.** (a) Characterization of AIG-vapor deposited MoS<sub>2</sub>. (i) AFM of monolayer MoS<sub>2</sub> with a trace showing an  $\sim 1$  nm film thickness (scale bar, 1  $\mu\text{m}$ ) and (ii) Raman spectroscopy of monolayer, bilayer, and few layer MoS<sub>2</sub> samples based on E<sub>2g</sub> and A<sub>1g</sub> peak separation. Adapted with permission from ref 108. Copyright American Chemical Society 2017. (b) Characterization of AIG-vapor deposited Bi<sub>2</sub>S<sub>3</sub>. (i) AFM image recorded from the sulfurized Bi<sub>2</sub>S<sub>3</sub> samples, with 1000 cycle Bi<sub>2</sub>O<sub>3</sub> thin film samples sulfurized at 500 °C and (ii) Raman spectra collected at room temperature from the sulfurized Bi<sub>2</sub>S<sub>3</sub> thin films grown on quartz substrates with Bi<sub>2</sub>O<sub>3</sub> thin films of different ALD cycles. Adapted with permission from ref 111. Copyright RSC 2014. (c) Characterization of AIG-vapor deposited MoSe<sub>2</sub>. (i) AFM image of three-layer MoSe<sub>2</sub> after transfer onto a SiO<sub>2</sub> substrate. (ii) Raman spectrum of the as-grown three-layer MoSe<sub>2</sub> nanosheet. The inset shows a schematic of Raman active vibration modes. Blue and orange balls represent Mo and Se atoms, respectively. Adapted with permission from ref 112. Copyright Springer 2018.

assisted layer (normally an oxide nanomembrane) prepared by ALD during the post-vapor treatment, as schematically shown in Figure 5b.<sup>107</sup> Therefore, it can be considered as a model of inducing the growth of TMD thin films derived from ALD. In order to study the advantages of AIG TMD materials, here in this chapter, we focus on (i) TMDs layers by AIG, (ii) the applications of the AIG TMDs, and (iii) the advantages and disadvantages of the route.

**3.1. AIG for TMDs: Materials and Mechanisms.** Kim's group from Yonsei University implemented the AIG method to fabricate the WS<sub>2</sub> film on SiO<sub>2</sub>/Si substrates with systematic layer controllability and wafer-level uniformity.<sup>107</sup> They ALD deposited a WO<sub>3</sub> film on the wafer first by using WH<sub>2</sub>(iPrCp)<sub>2</sub> and O<sub>2</sub> plasma as precursors, respectively, at 300 °C. Subsequently, they used the gas generated by the sublimation of sulfur powder in the H<sub>2</sub>S and Ar atmosphere to react with predeposited WO<sub>3</sub> to obtain a WS<sub>2</sub> film with a visually uniform outcome. The work provides preliminary evidence of the feasibility and practicality of the AIG approach in view of the

successful synthesis and developed applications. After that, some TMD developments including MoS<sub>2</sub>,<sup>108–110</sup> Bi<sub>2</sub>S<sub>3</sub>,<sup>111</sup> and MoSe<sub>2</sub><sup>112</sup> based on this method were reported. Martella et al.<sup>110</sup> fabricated MoS<sub>2</sub> layers via AIG-vapor by using ALD MoO<sub>x</sub> as the film precursor and investigated the properties of the products. The obtained MoS<sub>2</sub> shows the same granular nature as that of the molybdenum oxide precursor with a slight roughness increase. The study carried out the AIG method to provide an idea for the synthesis of MoS<sub>2</sub> and to explore the effect of the ALD oxide precursor on the product. Keller et al.<sup>108</sup> also applied the AIG-vapor strategy to fabricate large-area MoS<sub>2</sub> monolayers (AFM image in Figure 6a (i)). They found that the sulfur incorporation and molybdenum reduction at a low temperature, but higher temperatures are required for 2H crystal structure formation via the chemical analysis during a multistep thermal sulfur treatment. The Raman spectra (Panel (ii) of Figure 6a) give good consistency with the results of those traditional CVD-produced MoS<sub>2</sub>,<sup>113,114</sup> while the difference is less than 20 cm<sup>-1</sup> (19.7 cm<sup>-1</sup>). A well-behaved

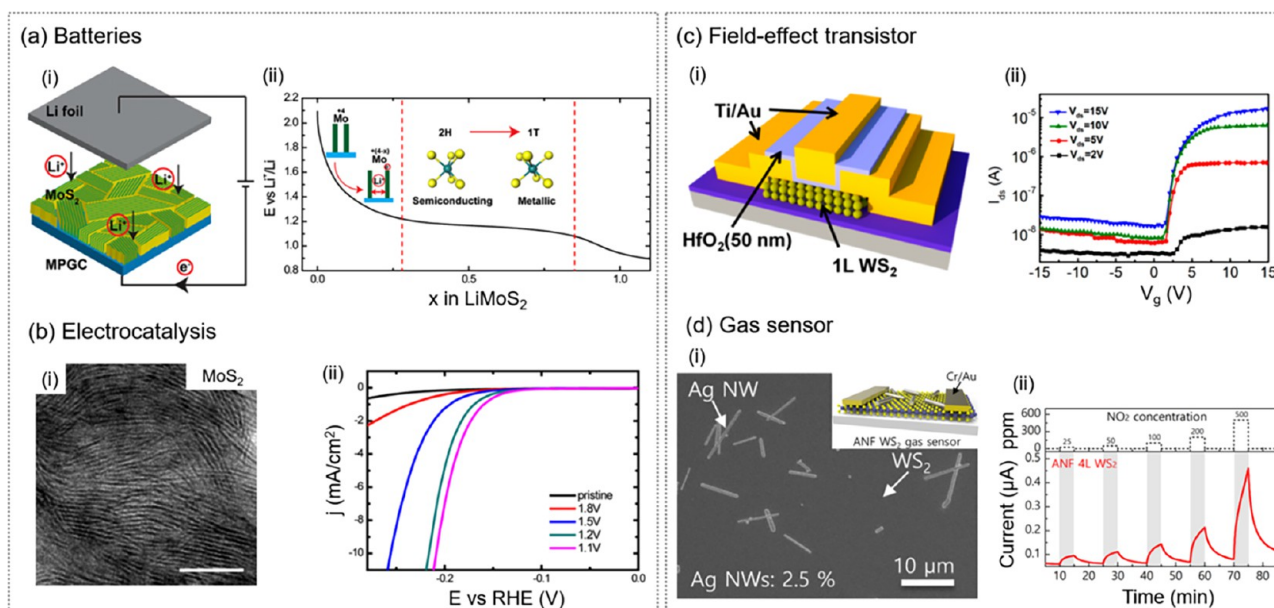


**Figure 7.** (a) AIG-vapor deposited MoS<sub>2</sub> for batteries. (i) Schematic of the battery testing system. The cathode is the MoS<sub>2</sub> film with molecular layers perpendicular to the substrate, where the green and yellow colors represent the edge sites and the terrace sites, respectively. (ii) Galvanostatic discharge curve representing the lithiation process. Reprinted with permission from ref 109. Copyright National Academy of Sciences 2013. (b) AIG-vapor deposited MoS<sub>2</sub> with Li intercalation for HER electrocatalysis. (i) TEM image of MoS<sub>2</sub> by Li electrochemical intercalation to 1.1 V vs Li<sup>+</sup>/Li. (ii) Polarization curves of pristine and lithiated MoS<sub>2</sub> on mirror polished glassy carbon, with the catalytic activities improved by lower voltage Li intercalation. Adapted with permission from ref 109. Copyright National Academy of Sciences 2013. (c) FET based on monolayer WS<sub>2</sub> deposited by AIG vapor. (i) Structure schematic on the monolayer WS<sub>2</sub>. (ii) Transfer curve for the FET. Reprinted with permission from ref 107. Copyright American Chemical Society 2013. (d) Gas sensor based on AIG-vapor deposited WS<sub>2</sub>. (i) Scanning electron microscopy image of the Ag nanowire-functionalized WS<sub>2</sub> film. (ii) Gas-sensing results of the Ag nanowire-functionalized WS<sub>2</sub> gas sensors consisting of a four-layer WS<sub>2</sub> film upon NO<sub>2</sub> exposure (25, 50, 100, 200, and 500 ppm). Adapted with permission from ref 119. Copyright American Chemical Society 2016.

layer control and uniformity for the wafer scale and the 2H-crystallization MoS<sub>2</sub> in the sequent nucleation step made this method an efficient growth method for synthesizing and tuning the product layer, simultaneously. The work also indicates that more improvements are required for an ideal growth. This may include the optimization of the parameters like the growth temperatures, the type of gas used, and the surface treatments of the ALD oxide nanomembrane, so that sub-1 nm nucleation control of the nucleation domains in the post-treatment can be achieved.<sup>108</sup>

Liu et al.<sup>111</sup> carried out some studies on another sulfur compound, Bi<sub>2</sub>S<sub>3</sub>, by using the AIG-vapor method. The Bi<sub>2</sub>O<sub>3</sub> film was deposited on different substrates by ALD first, and subsequently the samples were sulfurized. As the AFM image illustrated in Panel (i) of Figure 6b, the surface morphology of the 1000-ALD-cycles Bi<sub>2</sub>O<sub>3</sub> film after sulfurization on the Si substrate is granular at the nanoscale. The X-ray diffraction (XRD) patterns of sulfurized films with various cycles is highly matched with the theoretical orthorhombic Bi<sub>2</sub>S<sub>3</sub> pattern, suggesting the existence of the Bi<sub>2</sub>S<sub>3</sub> crystal. In addition, the five phono modes (P'1–P'5) in the Raman spectra (Panel (ii) of Figure 6b) are in accordance with the Raman active phonons of Bi<sub>2</sub>S<sub>3</sub> reported in previous work,<sup>115</sup> further providing clear-cut evidence that the Bi<sub>2</sub>O<sub>3</sub> layer was converted into the Bi<sub>2</sub>S<sub>3</sub> film after the sulfurization. It can also be observed that the scattering intensities increase with the nominal film thickness, which is determined by the number of ALD cycles (Panel (ii) of Figure 6b). Similar to the sulfide, selenide has also been developed via the AIG vapor route to achieve a high uniformity and controllability. Dai and collaborators synthesized layered MoSe<sub>2</sub> nanosheets (AFM

image in Panel (i) in Figure 6c) by selenizing the ALD-deposited MoO<sub>3</sub> film through the AIG method by using the selenium powder as a reactant under the H<sub>2</sub> and Ar atmosphere.<sup>112</sup> The three Raman modes (Panel (ii) of Figure 6c) clearly prove that the selenization can induce the nucleation of MoSe<sub>2</sub>.

Some studies concerning the growth mechanism of this inducing process have also been published. The first finding is that there exists a critical temperature during the transition reaction from oxide to sulfide. Grossman et al.<sup>108</sup> confirmed this in their study by analyzing the elements of MoS<sub>2</sub> samples prepared at different temperatures. Their results showed that the 2P peak of S is sharpened and a weak Raman signal emerges in the film fabricated at ~600 °C, which proves the initial formation of the MoS<sub>2</sub> crystal. Afterward, a large number of MoS<sub>2</sub> crystals would be formed when the temperature is more than 700 °C. When the temperature increases to 900 °C, the formation of the 2H phase MoS<sub>2</sub> is noticed.<sup>108</sup> Second, the work of Schwartzberg's group demonstrated that the humidity plays an important role in the growth of TMDs.<sup>116</sup> They found that the unintentional or intentional presence of water enhances the volatilization, and the vapor enhances the transportation of tungsten and molybdenum oxide. The results showed that, when using water vapor as an involvement of the sulfurization reaction, monolayer single-crystalline islands form under the water atmosphere which promoted the continuous growth of MoS<sub>2</sub>.<sup>116</sup> The latest research by Markeev et al.<sup>117</sup> found that MoS<sub>2</sub> with low crystallinity starts to appear when the temperature is close to 500 °C, while the grain growth occurs at 500–1000 °C. They divided the sulfurization process of inducing growth into two steps: a conversion and

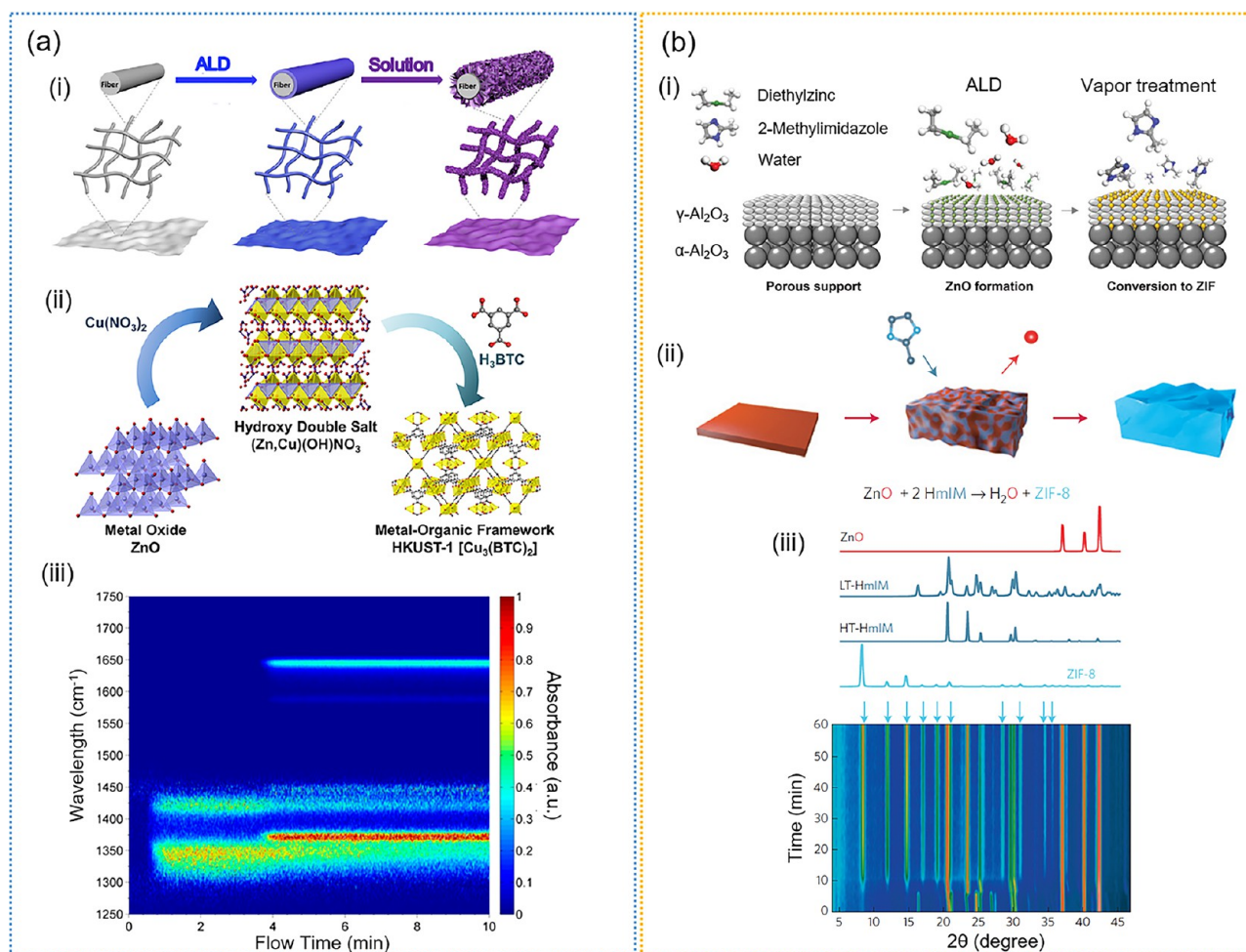


**Figure 8.** (a) Reaction procedures and mechanisms of AIG liquid. (i) Schematic illustration of a synthetic procedure of MOF/fiber textiles using ALD oxide-coated fibers, followed by reacting with organic linkers solutions. Adapted with permission from ref 146. Copyright Cell Press 2020. (ii) Schematic of the rapid room-temperature synthesis of HKUST-1. Reprinted with permission from ref 147. Copyright American Chemical Society 2015. (iii) Time-resolved infrared absorption spectra for surface reactions to form the HKUST-1 film. Adapted with permission from ref 149. Copyright American Chemical Society 2017. (b) Reaction procedures and mechanisms of AIG vapor. (i) Schematic of the all-vapor phase ZIF film fabrication process. Adapted with permission from ref 152. Copyright American Association for the Advancement of Science 2018. (ii) Schematic overview of the ZIF-8 film transformation mechanism. (iii) Plot of the time-resolved diffraction patterns viewed down the intensity axis, showing the transformation of crystalline phases in a 1:2 mixture of crystalline ZnO and 2-methylimidazole powder at 130 °C. Adapted with permission from ref 153. Copyright Springer Nature 2016.

crystallization step at  $\sim 500$ – $700$  °C and grain growth with the (0001) plane parallel to the substrate at over 900 °C. This also revealed that even the molybdenum oxide with a low melting point ( $\sim 795$  °C) can be converted to  $\text{MoS}_2$  in this reaction.<sup>117</sup> Besides, the researchers<sup>108,110,117</sup> also found that  $\text{MoS}_2$  conversion reaction is originally initiated by the elemental sulfur on the oxide surface. As the reaction temperature increases, the ionic bond between oxide layers and the elemental sulfur on the surface decreased, which contributed to the formation of the  $\text{MoS}_2$  film layers.

It can be concluded from this research that the properties and crystal quality of the final TMD product can be controlled by a variety of factors, including temperature, heating rate, and humidity.<sup>116</sup> The temperature gradient control plays a significant role in the crystallization of  $\text{MoS}_2$ ,<sup>108,110,117</sup> while influence from some other factors during AIG of TMDs may need further investigation.

### 3.2. AIG for TMDs: Applications and Performance.

Figure 7 exhibits the remarkable versatility of layered TMD materials by AIG, and their application examples in

batteries,<sup>109</sup> electrocatalysis,<sup>109</sup> field-effect transistors,<sup>107,118</sup> and gas sensors.<sup>91</sup> In the field of batteries (Figure 7a), Wang and colleagues developed vertically aligned  $\text{MoS}_2$  films on carbon fiber papers by AIG which was then used as the cathode of the Li-ion battery (Panel (i) of Figure 7a).<sup>109</sup> Panel (ii) of Figure 7a shows the electrochemical intercalation of  $\text{Li}^+$  in detail. It was found that  $\text{Li}^+$  intercalation in this battery could achieve the phase transition of the  $\text{MoS}_2$ , from the 2H phase to the 1T phase (semiconductor phase to metal phase transition). The obtained  $\text{LiMoS}_2$  film (corresponding transmission electron microscopy (TEM) image in Panel (i) of Figure 7b) was capable of improving the hydrogen evolution reaction (HER) performance, as shown in panel (ii) of Figure 7a. It can be observed that, compared with the pristine film,  $\text{MoS}_2$  films modified with lithium ions show better catalytic performance. The research demonstrates the advantage of synthesizing TMD films with accurate control of nanoscale structures (vertically aligned films) by AIG and the accessibility of fabricating materials on various substrates with readily diverse chemical or physical treatment (here in

this work is electrochemical insertion of lithium ions) to get new materials. It can be expected that one single TMD film on the substrate can be designed or functionalized with different scales, patterns, and properties through the AIG process.

Except for the energy related devices, a huge capacity in field effect transistors (FET) devices can also be found on ALD-based TMDs.<sup>48</sup> The AIG-vapor deposited WS<sub>2</sub> was assembled to a FET as the high-*k* dielectric gate insulator (Figure 7c (i)) by Kim's group.<sup>107</sup> Panel (ii) of Figure 7c shows the testing results of the device at the room temperature in air. The extracted field effect electron mobility is 3.9 cm<sup>2</sup>/(V s), and the subthreshold swing value is as low as 0.6 V/dec, both of which are comparable to the CVD MoS<sub>2</sub> device and exfoliated MoS<sub>2</sub> device, demonstrating the good quality of the WS<sub>2</sub> film produced by AIG.<sup>107</sup> Ko et al.<sup>119</sup> developed an Ag nanowire-decorated, large-area WS<sub>2</sub> nanosheet by AIG, using the ALD WO<sub>3</sub> as the induction layer and the H<sub>2</sub>S postsulfurization. By controlling the number of ALD cycles, WS<sub>2</sub> with different numbers of layers can be obtained. The four-layer WS<sub>2</sub> FET based gas sensor (shown in Panel (i) of Figure 7d) is able to show a dramatically improved response upon NO<sub>2</sub> exposure. As presented in Panel (ii) of Figure 7d, a 667% response of the NO<sub>2</sub> gas can be achieved, which can be attributed to the redox potential alteration of 2D TMDs and the promotion of adsorption of NO<sub>2</sub> molecules by generating intermediate states between the NO<sub>2</sub> gas phase and the adsorbed NO<sub>2</sub> on WS<sub>2</sub>.<sup>120</sup> It is noteworthy that TMD layers produced by both conventional ALD and AIG approaches were engaged in various applications including energy and electronics due to the precisely controllable size in nanoscale and high accessibility on different matrixes. The electronic structure changes of TMDs and interface effects brought about by these two advantages have also proved to be beneficial to the device performance.<sup>107,109,112</sup>

The above research advocates the utilization of the vapor phase method for postprocessing. It is probably because the vapor reaction steps are relatively simple, which facilitates the preparation of the uniform product with a large area. Besides, according to the research of Keller et al.<sup>108</sup> and Liu et al.,<sup>111</sup> the interface between the substrate and the ALD induction layer may affect the postprocessing steps, which plays a guiding role in the synthesis of another kind of layer materials. The process of AIG-vapor basically consists of the replacement of oxygen elements and the nucleation and crystallization growth of TMDs, which may require further detailed research and characterizations for full understanding of the mechanism. Nevertheless, it is clear that this approach could have enormous potential for large-scale fabrication of some other sulfide, selenide, or telluride and for flexible integration of these layered materials.

#### 4. MOF FILMS

Since the discovery of MOF materials,<sup>121–124</sup> they have been widely investigated because of their own properties such as large specific surface area, directional metal ion doping, and a stable carbon source.<sup>125–129</sup> It is because of these characteristics that MOF materials have been widely studied in the various fields such as energy,<sup>130–134</sup> separation,<sup>135–137</sup> and biology.<sup>138–141</sup> The conversion of MOFs from bulk material to layered material means that the application of MOFs can be enriched, especially in the field of integrated microelectronics and biosensors.<sup>142–144</sup> However, it is difficult to accurately produce MOF films by the conventional solvothermal method.

Some investigations have been developed on solvent coating methods to prepare MOFs films, which, however, could lead to the peeling of MOF particles.

##### 4.1. AIG for MOF Films: Process and Mechanisms.

Recently, some researchers have developed several promising methods to build stable and uniform MOF membranes via AIG-liquid or AIG-vapor. It is worth mentioning that Ahvenniemi and Karppinen developed a direct gas-phase route to produce a crystalline MOF thin film through ALD.<sup>145</sup> A highly crystalline copper(II)terephthalate (Cu-TPA) MOF thin film was fabricated by using Cu(thd)<sub>2</sub> (copper 2,2,6,6-tetramethyl-3,5-heptanedione) as the copper precursor and terephthalic acid (TPA) as the organic precursor, respectively.<sup>145</sup> The XRD pattern of the as-deposited film shows perfect consistency with the paddlewheel-type MOF-2 structure.<sup>145</sup> Obviously, the ALD technology itself contributes to the synthesis of membranes or layered materials, but the reports of direct synthesis of MOFs by ALD are relatively scarce at present, which requires intensive research on the development of the corresponding ALD precursors in the future.

Thus, as shown in Figure 8, here we focus on the emerging AIG strategies to fabricate MOF films from the two perspectives of different post-treatments, i.e., liquid (blue region) and vapor (canary yellow region) treatments. On one hand, by using the ALD technology to construct induction layers and further liquid-phase reaction growth, some large, uniform, and firm loads of MOF films on a variety of substrates (Panel (i) of Figure 8a show a schematic diagram of MOF preparation on fabric) has been successfully developed by the Parsons group.<sup>146</sup> Zhao et al.<sup>147</sup> synthesized a HKUST-1 film by using the AIG-liquid method at room temperature. As illustrated in Panel (ii) of Figure 8a, a new mechanism was proposed to explain the transformation and growth of the MOFs films. The ZnO membrane was deposited first using ALD and then transformed to (Zn, Cu) hydroxy double salt (HDS) after the reaction with copper nitrate.<sup>117</sup> Similar to layered double hydroxides (LDHs), the obtained HDSs are layered materials consisting of cationic sheets connected by inorganic/organic interlamellar anions.<sup>148</sup> Besides, an *in situ* time-resolved attenuated total reflectance infrared spectroscopy (Panel (iii) of Figure 8a) was applied to reveal the detailed reaction process of the nucleation of HKUST-1,<sup>149</sup> during which both the formation of HDSs and the conversion of HKUST-1 reactions follow the pseudo-first-order kinetics. However, AIG-liquid is not suitable for the preparation of MOFs under any conditions, especially when the substrate is vulnerable to the reaction environment (such as on the chip in the ultraclean environment). Liquid reaction and the traditional solvothermal method may also cause contamination and corrosion.<sup>150,151</sup> In view of this issue, vapor treatment has become another promising strategy to fabricate MOF films.

As mentioned above, a certain number of TMDs has been successfully synthesized by the AIG-vapor strategy. As illustrated in Panel (i) of Figure 8b, the AIG-vapor for MOFs generally consists of two steps: the deposition of the oxide induction layer and the sequent organic ligand vapor reaction, which is similar to the process in the case of TMDs but different in crystal growth.<sup>152</sup> Ameloot and colleagues first demonstrated the totally chemical vapor process to fabricate layered ZIF-8 by utilizing the ALD-ZnO film as the induction layer and 2-methylimidazole vapor-treatment.<sup>153</sup> The white powdery 2-methylimidazole was heated as the organic

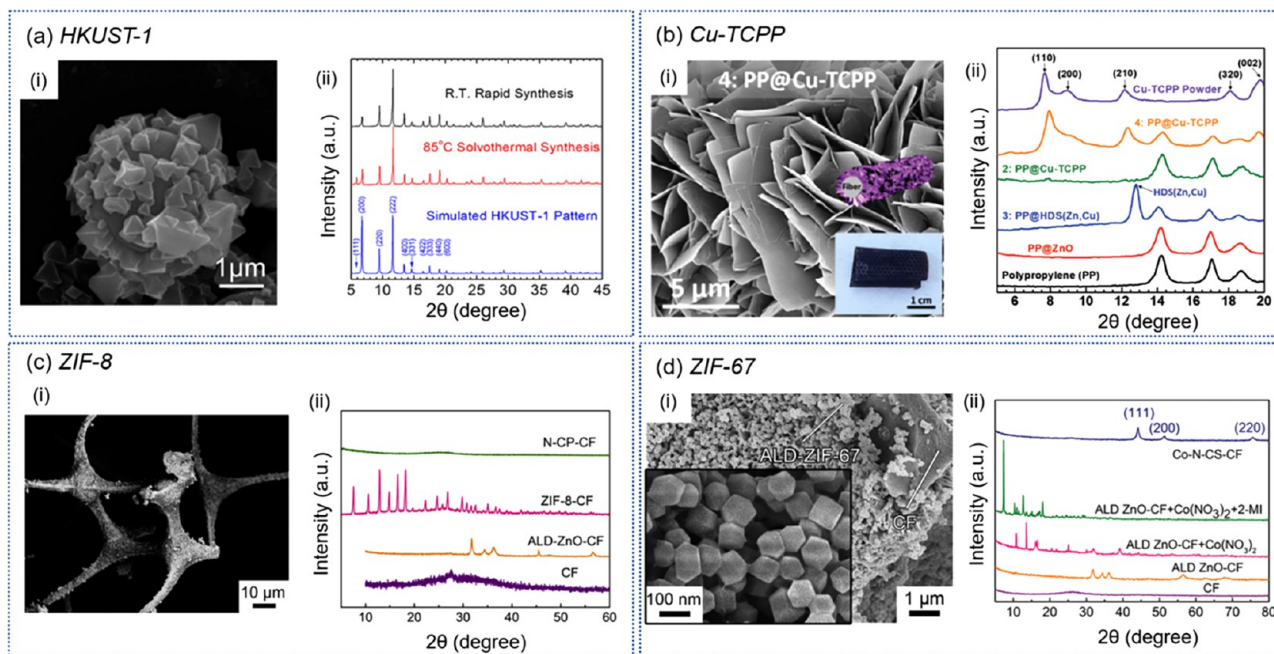


**Figure 9.** (a) HKUST-1 film deposited onto polystyrene spheres. (i) SEM image and (ii) XRD patterns. Adapted with permission from ref 147. Copyright American Chemical Society 2015. (b) Cu-TCPP film fabricated on polypropylene fibers. (i) SEM image and (ii) XRD patterns. Adapted with permission from ref 159. Copyright Wiley 2019. (c) ZIF-8 film coated on carbon foam. (i) SEM image and (ii) XRD patterns. Adapted with permission from ref 161. Copyright Elsevier 2020. (d) ZIF-67 film deposited on carbon foam. (i) SEM image and (ii) XRD patterns. Adapted with permission from ref 162. Copyright Wiley 2019.

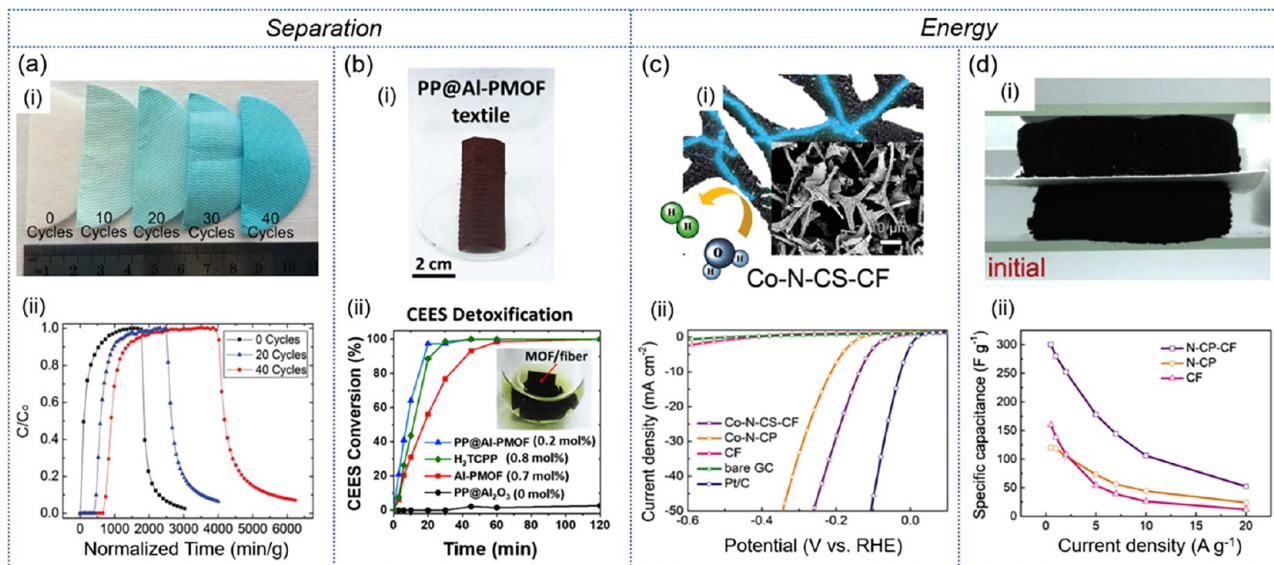


**Figure 10.** (a) HKUST-1 film deposited on polypropylene fibers. (i) Optical photo of HKUST-1 coated polypropylene fibers and (ii) NH<sub>3</sub> breakthrough curves for ALD HKUST-1 coated polypropylene fiber mat with different oxide cycles. Adapted with permission from ref 169. Copyright Royal Society of Chemistry 2015. (b) Al-PMOF film deposited on a polypropylene textile. (i) Optical photo of a colorimetric MOF/fiber textile and (ii) oxidation performance of CEES to CEESO conversion over time using varied photocatalysts. Reprinted with permission from ref 171. Copyright Cell Press 2020. (c) Co, N-codoped carbon sphere on 3D carbon foam derived from a ZIF-67 film. (i) Schematic illustration of the composite and (ii) HER performance of the samples. Adapted with permission from ref 162. Copyright Wiley 2019. (d) N-doped carbon particles on carbon foam derived from the ZIF-8 film. (i) Optical photo of the composite and (ii) specific capacitance of the corresponding electrodes at various current densities. Adapted with permission from ref 161. Copyright Elsevier 2020.

precursor, facing toward the as-deposited ZnO film, to get a sufficient vapor reaction in a closed reactor vessel.<sup>153</sup> It can be concluded as a typical AIG-vapor strategy by which the ZIF-8 film has been elegantly deposited without any solution involved. As the schematic displayed in Panel (ii) of Figure 8b, a new reaction mechanism called the neutralization

reaction was proposed to describe this AIG process. The *in situ* powder XRD patterns (Panel (iii) of Figure 8b) suggest that no phases other than 2-methylimidazole, zinc oxide, and ZIF-8 are detected at any time. By establishing a function between the mass fraction and reaction time of the vapor treatment, they also found that the neutralization reaction front

progressed deeper into the ZnO, thus mobilizing more Zn<sup>2+</sup> for MOF formation, before nucleation and growth of a continuous ZIF-8 film.<sup>153</sup>

Based on these ALD-derived principles, a number of MOF films on various substrates with different morphologies have been developed,<sup>154–158</sup> which inspired a wave of research on novel MOF film preparations and the extension of the ALD technique. Some examples of MOF films synthesized by AIG-liquid and AIG-vapor processes on various substrates are displayed in Figures 9 and 10.

**4.2. AIG-Liquid for MOF Films: Materials and Characterizations.** As shown in Figure 9a, a HKUST-1 film coating microsphere is fabricated by the AIG liquid process on a sphere matrix, by using the ALD ZnO as the induction layer and Cu(NO<sub>3</sub>)<sub>2</sub> and 1,3,5-benzenetricarboxylic acid (H<sub>3</sub>BTC) as liquid reactants at room temperature.<sup>147</sup> The obtained HKUST-1 film shows a well-behaved crystallization according to the XRD results (Panel (ii) of Figure 9a), in which the HKUST-1's patterns are in accordance with the simulated patterns. The MOF coating showed a stable adhesion because of the partially unconverted ZnO layer.<sup>147,149</sup>

Another example is the water-stable Cu-TCPP film anchored on a textile for chemical protection.<sup>159</sup> After the formation of HDS, the organic ligand TCPP (H<sub>2</sub>TCPP = 5,10,15,20-tetrakis(4-carboxyphenyl)porphyrin)<sup>159</sup> was used as the reactant to form the Cu-TCPP MOFs layer (Panel (i) of Figure 9b). Unlike the blue Cu-BTC, this MOF film is composed of aggregated nanosheets after crystallization and demonstrates a dark purple color. Besides, a typical Zr-based MOF, UiO-66, was also fabricated on textiles by carrying out the AIG-liquid route.<sup>160</sup> Its derivative, UiO-66-HH<sub>2</sub>, has also been successfully prepared and the related chemical properties and was studied by Lee and colleagues.<sup>160</sup> In addition, uniform and stable ZIF-8 and ZIF-67 films, two kinds of prototypical MOF materials, were synthesized on a flexible carbon foam via AIG-liquid by Zhao and collaborators (Figure 9c,d).<sup>161,162</sup> It can be found that these ZIF films are composed of stacked particles, and the geometry of the particles is a polyhedron, similar to the ZIF powder fabricated by the conventional route.<sup>163</sup> Meanwhile, good adhesion between the particles and the substrate has also been demonstrated due to the presence of the induction layer.<sup>161,162</sup> The corresponding XRD patterns (Panel (ii) in Figure 9c,d) indicate a good crystal feature of these MOF films.

**4.3. AIG-Liquid for MOF Films: Applications and Performance.** Due to the emergence of this AIG technology, some assembled devices based on MOF films have been developed and utilized. Figure 10 exhibits typical the applications and corresponding performances of these MOF-based structures, which are produced by the AIG-liquid strategy. Generally, MOFs were considered to have the potential for gas screening or gas separation because of its porous nature.<sup>121,164</sup> Thus, MOF films prepared by AIG also demonstrated remarkable achievements in this respect.<sup>165–168</sup>

Panel (i) of Figure 10a shows the optical image of a HKUST-1 film on a polypropylene fiber, as well as the corresponding mat on the centimeter scale.<sup>169</sup> It can be obviously observed that the color of the mat becomes darker with the increase of ALD-Al<sub>2</sub>O<sub>3</sub> cycles, indicating the amount of the HKUST-1 growth increases, which further explains the induction effect of the Al<sub>2</sub>O<sub>3</sub> layer. This MOF film-coated fiber mat was then utilized as an adsorption for hazardous gases including NH<sub>3</sub> and H<sub>2</sub>S.<sup>169</sup> The NH<sub>3</sub> breakthrough curves for

the 0, 20, and 40 cycle ALD-induced MOF film-coated fiber mats are illustrated in Panel (ii) of Figure 10a. It can be seen that the MOF film loaded fiber mat holds a better adsorption effect than the non-ALD mat, with the 40 cycles ALD-induced MOFs-coated mat giving breakthrough times of ~700 min g<sub>MOF+fiber</sub><sup>-1</sup> and ~4200 min g<sub>MOF</sub><sup>-1</sup>, which is closed (80%) to the previously reported solvothermal-MOF decorated fiber mat.<sup>169</sup> Besides, three Zr-based MOF films, UiO-66, UiO-66-NH<sub>2</sub>, and UiO-67 films, were synthesized on the fiber mats through the AIG-liquid way and utilized in the degradation of chemical warfare agents.<sup>170</sup> All three MOF film-coated fiber mats show the effective hydrolysis degradation of the nerve agent Soman, with its half-life being shortened to 2.3 min by the UiO-67-loaded mat. Similarly, a kind of Al-based MOF, Al-PMOF, was fabricated on a fiber mat as a protective film from sulfur mustard (Panel (i) of Figure 10b).<sup>171</sup> As displayed in Figure 10b, the Al-PMOF film-coated fiber mat enables an outstanding and rapid photocatalytic degradation of the sulfur mustard simulant 2-chloroethylethyl sulfide (CEES). The performance is better than that of the organic linker (H<sub>2</sub>TCPP) and the Al-PMOF powder. The detoxification conversion rate of the Al-PMOF-film-coated mat for CEES into a significantly less toxic product of 2-chloroethyl ethyl sulfoxide (CEESO) is up to 170 mol<sub>CEES</sub> mol<sup>-1</sup> chromophore min<sup>-1</sup> (Panel (ii) of Figure 10b), which is far higher than any other MOF films. As the assembly of MOF films grows more abundant, the development in these aspects is going to be accelerated.

Moreover, MOF films produced via the AIG-liquid approach have shown a significant capacity for energy-related applications, not only because of the unique properties of MOFs but also regarding the distinctive AIG process. For example, Zhao et al.<sup>161</sup> assembled the ZIF-67 film on carbon foam as mentioned before in Figure 8d. The obtained 3D foam was carbonized to get Co, N-codoped carbon spheres on carbon foam (Panel (i) of Figure 10c) for hydrogen evolution reaction (HER) electrocatalysis. Panel (ii) of Figure 10c exhibits the linear sweep voltammetry (LSV) results at a scan rate of 5 mV s<sup>-1</sup> in a 0.5 M H<sub>2</sub>SO<sub>4</sub> electrolyte. It should be noted that a better catalyst normally holds a lower overpotential at a particular current density, and 10 mA cm<sup>-2</sup> is usually adopted.<sup>161</sup> The results indicate that Co, N-co-doped carbon spheres on carbon foam show an excellent HER performance in terms of the overpotential of 142 mV at 10 mA cm<sup>-2</sup> and low Tafel slope of 73 mV dec<sup>-1</sup> in acid media, which can be ascribed to the large electrochemical surface of the carbonized ZIF structure. The long-term running test and repeated LSV test show well-behaved stability and durability of the composite, both of which are significant criteria for a HER electrocatalyst. Similarly, Zhao and colleagues developed a flexible capacitor of N-doped carbon particles on carbon foam by carbonizing the AIG-liquid ZIF-8-film-coated carbon foam.<sup>161</sup> Panel (i) of Figure 10d shows the initial state of the composite is flexible and can be pressed and rebound afterward.<sup>161</sup> The corresponding capacitor can further provide a stable capacitance 250 F g<sup>-1</sup> and a high energy density (17.36 W h kg<sup>-1</sup>) under a large deformation (25% of original thickness). As depicted in Panel (ii) of Figure 10d, the composite exhibits a higher capacitance rather than carbon foam and carbon particle individually, and this is attributed to the structural property of the composite where the large surface area and the firm and flexible support of the carbon foam are combined.

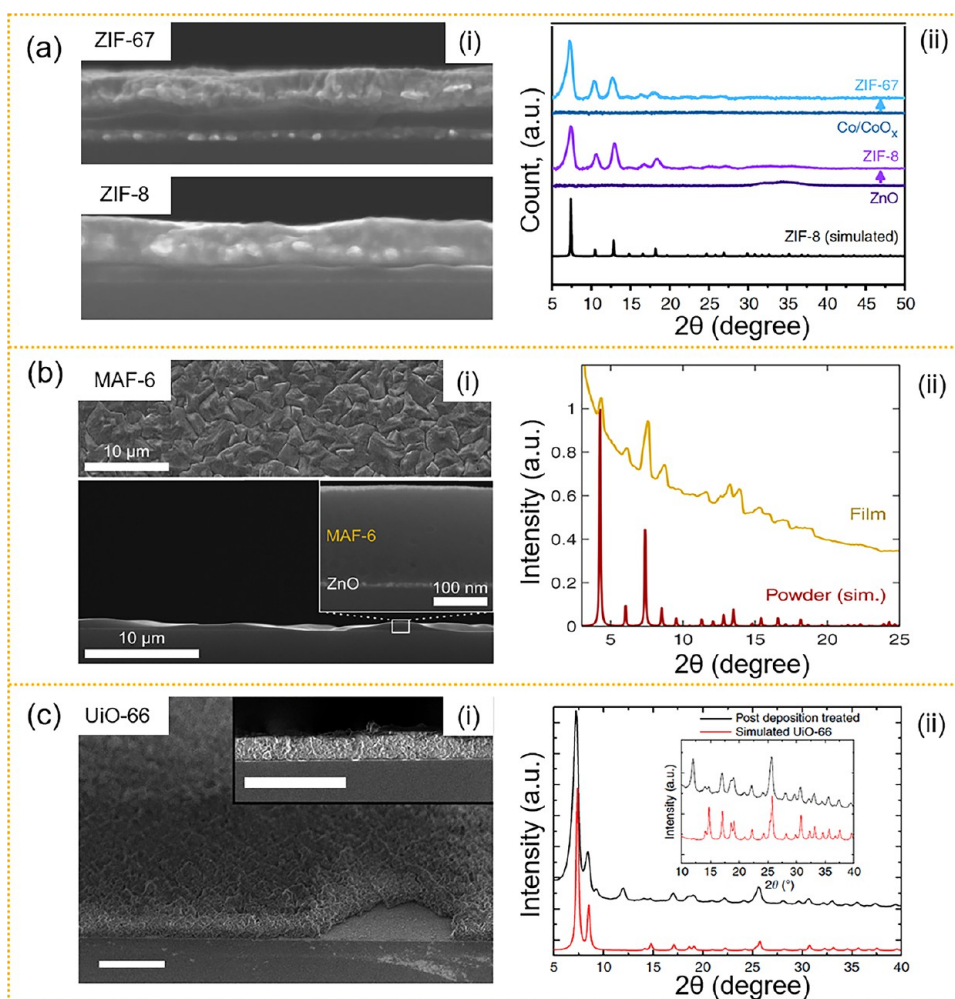


**Figure 11.** (a) AIG-vapor deposited ZIF-67 and ZIF-8 films. (i) Cross-sectional SEM images and (ii) corresponding XRD patterns. Adapted with permission from ref 180. Copyright Springer Nature 2019 (<http://creativecommons.org/licenses/by/4.0/>). The size of the characters in Panel (ii) of 11a has been modified. (b) AIG-vapor deposited MAF-6 thin film. (i) Cross-sectional SEM image and (ii) corresponding XRD results. Adapted with permission from ref 172. Copyright American Chemical Society 2020. (c) AIG-vapor deposited UiO-66 film. (i) Cross-sectional SEM image and (ii) corresponding XRD results. Adapted with permission from ref 174. Copyright Springer Nature 2016 (<http://creativecommons.org/licenses/by/4.0/>). The size of characters in Panel (ii) of 11c has been modified.

To sum up the AIG-liquid approach, it can be concluded that it is an effective and promising strategy for building MOFs with complex structures. The entire process usually requires an ALD induction layer, a metal ion source, and an organic ligand precursor. The cation reorganization between the induction layer and the metal ion source or the aggregation of the metal ion source on the induction layer is a key step in the whole reaction which may require further research to elucidate.<sup>147</sup> Besides, it is worth mentioning that the solvent of the liquid phase reaction plays a key role in the growth of MOFs, because it affects the bonding between the organic ligands and metal ions as well as the crystallization of MOFs.<sup>171</sup> The induction layer also provides a stable matrix for subsequent reactions and MOF growth. Some bottlenecks of conventional solvothermal methods for MOF synthesis have been broken such as complex reaction conditions, an uncontrollable process, and monotonous powdery-form products. As mentioned above, some MOF films including ZIFs, HKUST-1, and UiO-66 have been developed so far, while more MOFs films and other layered materials will come to our eyes through this way in the near future.

**4.4. AIG-Vapor for MOF Films: Materials and Characterizations.** In the meantime, some great achievements have been made through the AIG-vapor strategy, and a certain number of MOF films have been synthesized and developed.<sup>152,153,172–176</sup> In Figure 10, the morphologies of four kinds of MOF films deposited by AIG-vapor and the corresponding XRD characteristics are presented. In addition to ZIF-8 which is mentioned in the explanation of the AIG-vapor mechanism, ZIF-67 (Figure 11a) is also successfully fabricated by using the ALD-CoO as the induction layers.<sup>180</sup> It has been reported that similar MOFs including ZIF-61, ZIF-67, and ZIF-72 have been fabricated in the form of a thin film by adjusting the metal oxide layer.<sup>153</sup> Certainly, the organic precursor can also be exchanged to achieve different MOFs. A large-pore Zn-based MOF film, MAF-6 film (SEM image in Panel (i) of Figure 11b), was produced by using ALD ZnO and 2-ethylimidazole as the metal source and organic linkers, respectively.<sup>172</sup> The corresponding XRD pattern (Panel (ii) of Figure 11b) suggests a complete nucleation after the vapor phase reaction. The supercages of MAF-6 with a diameter at about 2 nm result in an exceptional uptake capacity of MAF-6 in comparison to ZIF-8, which is demonstrated by the vapor-

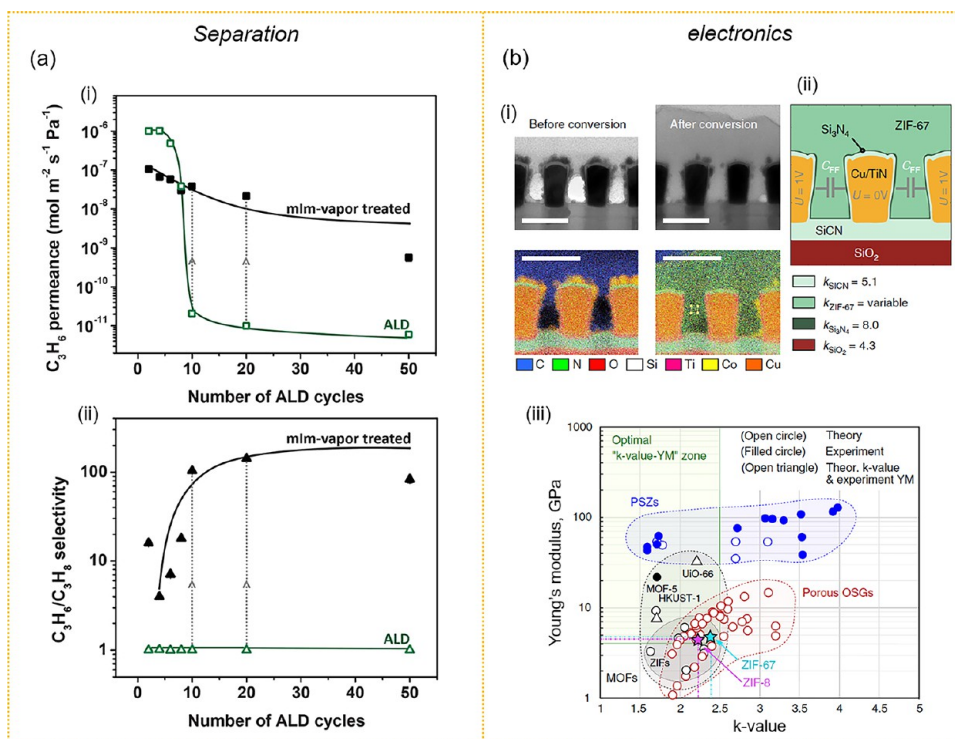


**Figure 12.** (a) Permeation performance of films during the ligand vapor treatment process. Propylene permeances (i) and propylene/propane single component selectivities (ii) of the ZIF-8/ $\gamma$ -alumina nanocomposite membranes as a function of the number of ALD cycles (solid symbols). Open symbols are values obtained from a support treated by the indicated cycles of ZnO ALD (before the ligand-vapor treatment). Reprinted with permission from ref 152. Copyright American Association for the Advancement of Science 2018. (b) Characterization and electric performance of the 45 nm half-pitch fork-fork capacitors coated with a ZIF-67 film. (i) TEM images and EDS elemental maps recorded on lamella cut out from the capacitor device. Scale bar is 100 nm. (ii) A 2D model of the device cross section employed for finite-element capacitance simulation. (iii) Positioning of MOFs on the Young's modulus/k-value map in comparison with other classes of advanced low-k dielectrics. Reprinted with permission from ref 180. Copyright Springer Nature 2019 (<http://creativecommons.org/licenses/by/4.0/>).

phase loading of a molecule larger than the ZIF-8 windows.<sup>172</sup> Moreover, five MOF films including Fe-BDC, Fe-BTC, Al-BDC, Al-BTC, and UiO-66 films have been synthesized through the AIG-vapor route for the solid-phase micro-extraction arrow for the first time.<sup>173</sup>  $\text{Al}_2\text{O}_3$  and  $\text{Fe}_2\text{O}_3$  layers were deposited by ALD as the metal precursors for Al-based MOFs films and Fe-based MOFs films, respectively, while the UiO-66 film was achieved by the post-chemical conversion of the ALD Zr-BDC film. Notably, a special thermal desorption unit was homemade and applied to the vapor treatment process. It shows a significant sealing effect, the same as that of the vessel used by Stassen et al.<sup>153</sup> Regarding to the UiO-66, actually, it was Nilsen's group<sup>174</sup> who pioneered the fabrication of the UiO-66 film by carrying out the AIG-vapor strategy and did detailed investigations. The ALD Zr-BDC layer was deposited using  $\text{ZrCl}_4$  and 1,4-benzenedicarboxylic acid as precursors. It can be inferred that the crystallization of UiO-66 film could be gained through the acetic acid vapor treatment from the XRD patterns (Panel (ii) of Figure 11c). As seen in the SEM image of the UiO-66 film displayed in Panel (i) of Figure 11c, excellent thickness controllability can be achieved which shows the superiority of this all-gas method compared with conventional wet methods.

**4.5. AIG-Vapor for MOF Films: Applications and Performance.** The cases summarized above mainly focus on the research of the AIG-vapor strategy and the synthesis of materials. Here in this section, some achievements of AIG-vapor MOF films have been concluded. Tsapatsis et al.<sup>152</sup> studied the selective permeability and the separation of the

AIG-vapor ZIF-8 film. At the same time, the permselectivity of the film can be utilized as an effective tool to identify the growth of MOFs films. As shown in Panels (i) and (ii) of Figure 12a, the ligand vapor-treated ZIF-8 film obtained from the ZnO layer shows a stable performance with a high propylene flux ( $>10^{-8} \text{ mol Pa}^{-1} \text{ m}^{-2} \text{ s}^{-1}$ ) and high mixture separation factor ( $\sim 100$ ) for propylene over propane (an energy-intensive high-volume separation), especially when the ALD cycles were set over 10 to 20. Here, the authors successfully demonstrated the utilization of the selective permeability of the ligand gas to guide the growth of the film and, in fact, conversely validated that the ZIF film prepared by the AIG-vapor method could behave with an excellent gas separation performance.<sup>152</sup> In addition, due to the limitations of traditional wet preparation methods, MOFs materials have been difficult to apply in the field of microelectronics. The most typical problem is that it is difficult to integrate powdery MOFs onto micrometer or nanometer-level devices.<sup>177–179</sup> Recently, progress on this issue has been reported by Krishtab and colleagues who first carried out the AIG-vapor strategy for the integration of ZIF-8 and ZIF-67 films as gap-filling low-k dielectrics in advanced on-chip interconnects.<sup>180</sup> The conversion result (TEM images and corresponding elemental distributions) of the ZIF-67 film, on lamella cut out from the fork-fork capacitor device, can be observed clearly from Panels (i) and (ii) of Figure 12b, comparing with the status before vapor treatment. Noteworthy, both the AIG-vapor prepared ZIF-67 and ZIF-8 films show Young's moduli and dielectric constants comparable to state-

of-the-art porous organosilica dielectrics (Panel (iii) of Figure 12b). It should be stressed that even though ZIFs are equivalent to the most advanced dielectrics in terms of mechanical and dielectric properties, the deposition via the AIG-vapor process demonstrates the distinct advantage of gap filling and therefore should be beneficial to future microelectronics integration projects.

Table 1 systematically shows recent research concerning the synthesis of MOFs with different geometries by using the AIG

**Table 1. Studies for the MOFs Prepared by the AIG Process**

material	method	structure	application	ref
HKUST-1	AIG-liquid	fiber@MOF, sphere@MOF, Si@MOF	gas capture	147
Cu-TCPP	AIG-liquid	fiber@MOF	gas capture	159
ZIF-67	AIG-liquid	sponge@MOF	electrocatalysis	161
ZIF-8	AIG-liquid	sponge@MOF	electrochemical sensor	162
HKUST-1	AIG-liquid	fiber@MOF	gas capture	165
ZIF-8, MIL-53-NH <sub>2</sub>	AIG-liquid	fiber@MOF	—	166
HKUST-1	AIG-liquid	multilayer fiber@MOF, PET@MOF	gas capture	169
UiO-66, UiO-66-NH <sub>2</sub> , UiO-67	AIG-liquid	fiber@MOF	toxicant degradation	170
Al-PMOF	AIG-liquid	Mat@MOF	toxicant degradation	171
Cu-BTC	AIG-liquid	fiber@MOF	—	181
UiO-66-NH <sub>2</sub>	AIG-liquid	Mat@MOF	toxicant degradation	182
MOF-525	AIG-liquid	fiber@MOF	toxicant degradation	183
ZIF-8	AIG-vapor	thin film	gas separation	152
ZIF-8	AIG-vapor	thin film	—	153
UiO-66-NH <sub>2</sub>	AIG-vapor	thin film	—	155
Cu-CDC	AIG-vapor	thin film	—	156
Zr-MOF	AIG-vapor	thin film	—	158
MAF-6	AIG-vapor	thin film	—	172
Fe-BTC, Fe-BDC, Al-BTC, Al-BDC, UiO-66	AIG-vapor	thin film	solid-phase extraction	173
UiO-66	AIG-vapor	thin film	—	174
MAF-252	AIG-vapor	thin film	—	176
ZIF-67, ZIF-8	AIG-vapor	thin film	low- <i>k</i> dielectric	180

process. According to the outcome of these studies, some significant comments can be proposed. First, unlike the AIG-liquid approach, the metal ions of the MOFs are totally determined by the ALD precursors in the AIG-vapor approach. Second, some results have indicated that the environment of the post-treatment such as temperature, humidity, duration, and pressure could affect the crystallization of MOFs, which means some further investigations should be implemented in the future. Moreover, it can be inferred that the AIG-vapor

approach has great potential for MOF-based devices in various fields such as sensors and biotechnology.

## 5. CONCLUSION AND PERSPECTIVE

Generally, considerable developments and progress have been made on layered materials by ALD so far, including the diversity of structures and types. The lift-off ALD method demonstrates its viability to prepare free-standing nanomembrane materials by releasing the deposited nanomembrane from the sacrificial substrate. A wide range of nanomembranes including single component, multicomponent, oxide/carbon composites, and organic/inorganic bilayer nanomembranes have been prepared by the lift-off ALD method, with well-controlled film thickness, composition, and crystalline phase. The free-standing membranes hold the advantages of uniformity and controllability of the traditional ALD films, and simultaneously it can also break the confinement that the traditional membranes are attached to the substrate, which enormously promotes the availability to applications in various fields, such as catalysis, energy conversion, and photovoltaic devices. This is because these films can be adjusted sufficiently freely without considering the tolerance of the substrate, as well as maintain good integrity. Besides, it is helpful that their intrinsic properties are not influenced and limited, and therefore, full play of their functionalities can be achieved. It can be predicted that such methods may be popularized for preparing other kinds of free-standing layered materials and can be applied in more fields like robotics and biology.

The ALD-derived fabrication of TMD layers and MOF films shows excellent capacity in a variety of domains from energy to microelectronics. Besides, the research and development of AIG technology has made the traditional ALD further improved, and more types of materials have been prepared on various types of substrates. This is equivalent to the evolution of the ALD technology achievement library, and more applications and new materials will be expected. On the other hand, the research concerning the growth mechanism, especially *in situ* investigation, including crystal growth during the AIG process and the impacts of reaction conditions to the products, is still insufficient. For example, in what ways does the temperature of the postreaction affect the formation of the products and their properties? In what ways is the coordination of the metal ions formed during the crystallization of the MOF? The preparation of new MOF films by AIG and analyses of physical and chemical properties of them also need future investigations. In summary, we believe that the content in this review will promote research in many fields and inspire more research on ALD technology and related materials. It can be expected that more interesting and exciting stories related to these methods and materials will happen in the community.

## ■ AUTHOR INFORMATION

### Corresponding Author

Yongfeng Mei — Department of Materials Science, Fudan University, Shanghai 200433, P.R. China; [orcid.org/0000-0002-3314-6108](https://orcid.org/0000-0002-3314-6108); Email: [yfm@fudan.edu.cn](mailto:yfm@fudan.edu.cn)

### Authors

Zhiwei Zhang — Department of Materials Science, Fudan University, Shanghai 200433, P.R. China  
Yuting Zhao — Department of Materials Science, Fudan University, Shanghai 200433, P.R. China

Zhe Zhao – Department of Materials Science, Fudan University, Shanghai 200433, P.R. China

Gaoshan Huang – Department of Materials Science, Fudan University, Shanghai 200433, P.R. China; [orcid.org/0000-0002-0525-7177](https://orcid.org/0000-0002-0525-7177)

Complete contact information is available at:  
<https://pubs.acs.org/10.1021/acs.chemmater.9b04414>

### Author Contributions

<sup>†</sup>Z.W.Z. and Y.T.Z. contributed equally.

### Author Contributions

Y.F.M. conceived the concept. All the authors discussed the text and commented on the manuscript.

### Notes

The authors declare no competing financial interest.

### ACKNOWLEDGMENTS

This work was supported by the National Natural Science Foundation of China (No. 51961145108 and 61975035) and the Science and Technology Commission of Shanghai Municipality (No. 19XD1400600 and 20501130700).

### REFERENCES

- (1) Liu, L. C.; Corma, A. Metal Catalysts for Heterogeneous Catalysis: From Single Atoms to Nanoclusters and Nanoparticles. *Chem. Rev.* **2018**, *118*, 4981–5079.
- (2) Jiao, L.; Wang, Y.; Jiang, H.-L.; Xu, Q. Metal-Organic Frameworks as Platforms for Catalytic Applications. *Adv. Mater.* **2018**, *30*, 1703663.
- (3) Wang, Y. L.; Sun, S. Y.; Zhang, Z. Y.; Shi, D. L. Nanomaterials for Cancer Precision Medicine. *Adv. Mater.* **2018**, *30*, 1705660.
- (4) Meng, Z.; Stolz, R. M.; Mendecki, L.; Mirica, K. A. Electrically-Transduced Chemical Sensors Based on Two-Dimensional Nanomaterials. *Chem. Rev.* **2019**, *119*, 478–598.
- (5) Zhou, G. M.; Xu, L.; Hu, G. W.; Mai, L. Q.; Cui, Y. Nanowires for Electrochemical Energy Storage. *Chem. Rev.* **2019**, *119*, 11042–11109.
- (6) Heard, C. J.; Cejka, J.; Opanasenko, M.; Nachtigall, P.; Centi, G.; Perathoner, S. 2D Oxide Nanomaterials to Address the Energy Transition and Catalysis. *Adv. Mater.* **2019**, *31*, 1801712.
- (7) Gong, C. H.; Hu, K.; Wang, X. P.; Wangyang, P. H.; Yan, C. Y.; Chu, J. W.; Liao, M.; Dai, L. P.; Zhai, T. Y.; Wang, C.; Li, L.; Xiong, J. 2D Nanomaterial Arrays for Electronics and Optoelectronics. *Adv. Funct. Mater.* **2018**, *28*, 1706559.
- (8) Shi, Y. M.; Li, H. N.; Li, L. J. Recent Advances in Controlled Synthesis of Two-Dimensional Transition Metal Dichalcogenides via Vapour Deposition Techniques. *Chem. Soc. Rev.* **2015**, *44*, 2744–2756.
- (9) Tan, C.; Zhang, H. Wet-Chemistry Synthesis and Applications of Non-Layer Structured Two-Dimensional Nanomaterials. *Nat. Commun.* **2015**, *6*, 7873.
- (10) Das, A.; Ganguli, A. K. Design of Diverse Nanostructures by Hydrothermal and Microemulsion Routes for Electrochemical Water Splitting. *RSC Adv.* **2018**, *8*, 25065–25078.
- (11) Thein, M. T.; Pung, S. Y.; Aziz, A.; Itoh, M. Stacked ZnO Nanorods Synthesized by Solution Precipitation Method and Their Photocatalytic Activity Study. *J. Sol-Gel Sci. Technol.* **2015**, *74*, 260–271.
- (12) Parashar, M.; Shukla, V. K.; Singh, R. Metal Oxides Nanoparticles via Sol-Gel Method: A Review on Synthesis, Characterization and Applications. *J. Mater. Sci.: Mater. Electron.* **2020**, *31*, 3729–3749.
- (13) Wang, F.; Seo, J.-H.; Ma, Z. Q.; Wang, X. D. Substrate-Free Self-Assembly Approach toward Large-Areal Nanomembranes. *ACS Nano* **2012**, *6*, 2602–2609.
- (14) Teixeira, I. F.; Barbosa, E. C. M.; Tsang, S. C. E.; Camargo, P. H. C. Carbon Nitrides and Metal Nanoparticles: from Controlled Synthesis to Design Principles for Improved Photocatalysis. *Chem. Soc. Rev.* **2018**, *47*, 7783–7817.
- (15) Johnson, R. W.; Hultqvist, A.; Bent, S. F. A Brief Review of Atomic Layer Deposition: from Fundamentals to Applications. *Mater. Today* **2014**, *17*, 236–246.
- (16) Knez, M.; Nielsch, K.; Niinistö, L. Synthesis and Surface Engineering of Complex Nanostructures by Atomic Layer Deposition. *Adv. Mater.* **2007**, *19*, 3425–3438.
- (17) Kim, H.; Lee, H. B. R.; Maeng, W. J. Applications of Atomic Layer Deposition to Nanofabrication and Emerging Nanodevices. *Thin Solid Films* **2009**, *517*, 2563–2580.
- (18) Poodt, P.; Knaepen, R.; Illiberi, A.; Roozeboom, F.; van Asten, A. Low Temperature and Roll-to-roll Spatial Atomic Layer Deposition for Flexible Electronics. *J. Vac. Sci. Technol., A* **2012**, *30*, No. 01A142.
- (19) Yu, F.; Du, L.; Zhang, G. X.; Su, F. M.; Wang, W. C.; Sun, S. H. Electrode Engineering by Atomic Layer Deposition for Sodium-Ion Batteries: from Traditional to Advanced Batteries. *Adv. Funct. Mater.* **2020**, *30*, 1906890.
- (20) Skoog, A. A.; Elam, J. W.; Narayan, R. J. Atomic Layer Deposition: Medical and Biological Applications. *Int. Mater. Rev.* **2013**, *58*, 113–129.
- (21) Puurunen, R. L. Surface Chemistry of Atomic Layer Deposition: A Case Study for The Trimethylaluminum/Water Process. *J. Appl. Phys.* **2005**, *97*, 121301.
- (22) Schwartzberg, A. M.; Olynick, D. Complex Materials by Atomic Layer Deposition. *Adv. Mater.* **2015**, *27*, 5778–5784.
- (23) Cai, J. Y.; Sun, Q.; Meng, X. B. Novel Nanostructured Materials by Atomic and Molecular Layer Deposition. *AIMS Mater. Sci.* **2018**, *5*, 957–999.
- (24) Biyikli, N.; Haider, A. Atomic Layer Deposition: An Enabling Technology for The Growth of Functional Nanoscale Semiconductor. *Semicond. Sci. Technol.* **2017**, *32*, No. 093002.
- (25) Hämäläinen, J.; Ritala, M.; Leskelä, M. Atomic Layer Deposition of Noble Metals and Their Oxides. *Chem. Mater.* **2014**, *26*, 786–801.
- (26) Mackus, A. J. M.; Schneider, J. R.; MacIsaac, C.; Baker, J. G.; Bent, S. F. Synthesis of Doped, Ternary, and Quaternary Materials by Atomic Layer Deposition. *Chem. Mater.* **2019**, *31*, 1142–1183.
- (27) De Pauli, M.; Malachias, A.; Westfahl, H.; Bettini, J.; Ramirez, A.; Huang, G. S.; Mei, Y. F.; Schmidt, O. G. Study of Roughness Evolution and Layer Stacking Faults in Short-Period Atomic Layer Deposited HfO<sub>2</sub>/Al<sub>2</sub>O<sub>3</sub> Multilayers. *J. Appl. Phys.* **2011**, *109*, No. 063524.
- (28) Tan, W.; Hendricks, O. L.; Meng, A. C.; Braun, M. R.; McGehee, M. D.; Chidsey, C. E. D.; McIntyre, P. C. Atomic Layer Deposited TiO<sub>2</sub>-IrO<sub>x</sub> Alloy as A Hole Transport Material for Perovskite Solar Cells. *Adv. Mater. Interfaces* **2018**, *5*, 1800191.
- (29) Geng, Y.; Guo, Li.; Xu, S. S.; Sun, Q. Q.; Ding, S. J.; Lu, H. L.; Zhang, D. W. Influence of Al Doping on The Properties of ZnO Thin Films Grown by Atomic Layer Deposition. *J. Phys. Chem. C* **2011**, *115*, 12317–12321.
- (30) Na, J.-S.; Peng, Q.; Scarel, G.; Parsons, G. N. Role of Gas Doping Sequence in Surface Reactions and Dopant Incorporation During Atomic Layer Deposition of Al-Doped ZnO. *Chem. Mater.* **2009**, *21*, 5585–5593.
- (31) Wu, Y.; Potts, S. E.; Hermkens, P. M.; Knoops, H. C. M.; Roozeboom, F.; Kessels, W. M. M. Enhanced Doping Efficiency of Al-Doped ZnO by Atomic Layer Deposition Using Dimethylaluminum Isopropoxide as An Alternative Aluminum Precursor. *Chem. Mater.* **2013**, *25*, 4619–4622.
- (32) Yanguas-Gil, A.; Peterson, K. E.; Elam, J. W. Controlled Dopant Distribution and Higher Doping Efficiencies by Surface-Functionalyzed Atomic Layer Deposition. *Chem. Mater.* **2011**, *23*, 4295–4297.
- (33) Lee, S. W.; Han, J. H.; Han, S.; Lee, W.; Jang, J. H.; Seo, M.; Kim, S. K.; Dussarrat, C.; Gatineau, J.; Min, Y. S.; Hwang, C. S. Atomic Layer Deposition of SrTiO<sub>3</sub> Thin Films with Highly

Enhanced Growth Rate for Ultrahigh Density Capacitors. *Chem. Mater.* **2011**, *23*, 2227–2236.

(34) Ritala, M.; Kukli, K.; Rahtu, A.; Raisanen, P.; Leskela, M.; Sajavaara, T.; Keinonen, J. Science Atomic Layer Deposition of Oxide Thin Films with Metal Alkoxides as Oxygen Sources. *Science* **2000**, *288*, 319–321.

(35) Meng, X.; Byun, Y.; Kim, H.; Lee, J.; Lucero, A.; Cheng, L.; Kim, J. Atomic Layer Deposition of Silicon Nitride Thin Films: A Review of Recent Progress, Challenges, and Outlooks. *Materials* **2016**, *9*, 1007.

(36) Lim, B.; Rahtu, A.; Gordon, R. Atomic Layer Deposition of Transition Metals. *Nat. Mater.* **2003**, *2*, 749–753.

(37) Huang, G. S.; Mei, Y. F. Thinning and Shaping Solid Films into Functional and Integrative Nanomembranes. *Adv. Mater.* **2012**, *24*, 2517–2546.

(38) Rogers, J. A.; Lagally, M. G.; Nuzzo, R. G. Synthesis, assembly and applications of semiconductor nanomembranes. *Nature* **2011**, *477*, 45–53.

(39) Cavallo, F.; Lagally, M. G. Semiconductors Turn Soft: Inorganic Nanomembranes. *Soft Matter* **2010**, *6*, 439–455.

(40) Huang, G. S.; Mei, Y. F. Assembly and Self-Assembly of Nanomembrane Materials-From 2D to 3D. *Small* **2018**, *14*, 1703665.

(41) Zanghelini, F.; Frías, I. A. M.; Rêgo, M. J. B. M.; Pitta, M. G. R.; Saciloti, M.; Oliveira, M. D. L.; Andrade, C. A. S. Biosensing Breast Cancer Cells Based on A Three-Dimensional TiO<sub>2</sub> Nanomembrane Transducer. *Biosens. Bioelectron.* **2017**, *92*, 313–320.

(42) Medina-Sánchez, M.; Ibarlucea, B.; Pérez, N.; Karnausenko, D. D.; Weiz, S. M.; Baraban, L.; Cuniberti, G.; Schmidt, O. G. High-Performance Three-Dimensional Tubular Nanomembrane Sensor for DNA Detection. *Nano Lett.* **2016**, *16*, 4288–4296.

(43) Liu, J.; Liu, X. W. Two-Dimensional Nanoarchitectures for Lithium Storage. *Adv. Mater.* **2012**, *24*, 4097–4111.

(44) Zhao, Z.; Kong, Y.; Zhang, Z.; Huang, G.; Mei, Y. Atomic Layer-Deposited Nanostructures and Their Applications in Energy Storage and Sensing. *J. Mater. Res.* **2020**, *35*, 701–719.

(45) Ma, F.; Yang, B.; Zhang, Z.; Kong, J.; Huang, G.; Mei, Y. Self-Rolled TiO<sub>2</sub> Microscroll/Graphene Composite for Electrochemical Dopamine Sensing. *Prog. Nat. Sci.* **2020**, *30*, 337–342.

(46) Lee, K.; Kim, D. H.; Parsons, G. N. Free-Floating synthetic Nanosheets by Atomic Layer Deposition. *ACS Appl. Mater. Interfaces* **2014**, *6*, 10981–10985.

(47) Lee, K.; Losego, M. D.; Kim, D. H.; Parsons, G. N. High Performance Photocatalytic Metal Oxide Synthetic Bi-component Nanosheets Formed by Atomic Layer Deposition. *Mater. Horiz.* **2014**, *1*, 419.

(48) Choi, W.; Choudhary, N.; Han, G. H.; Park, J.; Akinwande, D.; Lee, Y. H. Recent Development of Two-dimensional Transition Metal Dichalcogenides and Their Applications. *Mater. Today* **2017**, *20*, 116–130.

(49) Li, H.; Li, Y.; Aljarb, A.; Shi, Y.; Li, L. J. Epitaxial Growth of Two-Dimensional Layered Transition-Metal Dichalcogenides: Growth Mechanism, Controllability, and Scalability. *Chem. Rev.* **2018**, *118*, 6134–6150.

(50) Furukawa, H.; Cordova, K. E.; O’Keeffe, M.; Yaghi, O. M. The Chemistry and Applications of Metal-Organic Frameworks. *Science* **2013**, *341*, 1230444.

(51) Lin, K. S.; Adhikari, A.; Ku, C. N.; Chiang, C.; Kuo, H. Synthesis and Characterization of Porous HKUST-1 Metal Organic Frameworks for Hydrogen Storage. *Int. J. Hydrogen Energy* **2012**, *37*, 13865–13871.

(52) Cavka, J.; Jakobsen, S.; Olsbye, U.; Guillou, N.; Lamberti, C.; Bordiga, S.; Lillerud, K. A New Zirconium Inorganic Building Brick Forming Metal Organic Frameworks With Exceptional Stability. *J. Am. Chem. Soc.* **2008**, *130* (42), 13850–13851.

(53) Manzeli, S.; Ovchinnikov, D.; Pasquier, D.; Yazyev, O. V.; Kis, A. 2D Transition Metal Dichalcogenides. *Nat. Rev. Mater.* **2017**, *2*, 17033.

(54) Zhao, J.; Nunn, T. W.; Lemaire, C. P.; Lin, Y.; Dickey, D. M.; Oldham, J. C.; Walls, J. H.; Peterson, W. G.; Losego, D. M.; Parsons,

N. G. Facile Conversion of Hydroxy Double Salts to Metal–Organic Frameworks Using Metal Oxide Particles and Atomic Layer Deposition Thin-Film Templates. *J. Am. Chem. Soc.* **2015**, *137*, 13756–13759.

(55) Lausund, B. K.; Nilsen, O. All-Gas-Phase Synthesis of UiO-66 Through Modulated Atomic Layer Deposition. *Nat. Commun.* **2016**, *7*, 13578.

(56) Cai, J.; Han, X.; Wang, X.; Meng, X. Atomic Layer Deposition of Two-Dimensional Layered Materials: Processes, Growth Mechanisms, and Characteristics. *Matter* **2020**, *2*, 587–630.

(57) Ma, R. Z.; Sasaki, T. Nanosheets of Oxides and Hydroxides: Ultimate 2D Charge-Bearing Functional Crystallites. *Adv. Mater.* **2010**, *22*, 5082–5104.

(58) Stock, N.; Biswas, S. Synthesis of Metal-Organic Frameworks (MOFs): Routes to Various MOF Topologies, Morphologies, and Composites. *Chem. Rev.* **2012**, *112* (2), 933–969.

(59) Mei, J.; Liao, T.; Sun, Z. Q. Two-Dimensional Metal Oxide Nanosheets for Rechargeable Batteries. *J. Energy Chem.* **2018**, *27*, 117–127.

(60) Zhao, M. T.; Huang, Y.; Peng, Y. W.; Huang, Z. Q.; Ma, Q. L.; Zhang, H. Two-Dimensional Metal-Organic Framework Nanosheets: Synthesis and Applications. *Chem. Soc. Rev.* **2018**, *47*, 6267–6295.

(61) Yang, B. W.; Chen, Y.; Shi, J. L. Material Chemistry of Two-dimensional Inorganic Nanosheets in Cancer Theranostics. *Chem.* **2018**, *4*, 1284–1313.

(62) Seo, J.-H.; Swinnick, E.; Zhang, Y.-Y.; Kim, M. Low Dimensional Freestanding Semiconductors for Flexible Optoelectronics: Materials, Synthesis, Process, and Applications. *Mater. Res. Lett.* **2020**, *8*, 123–144.

(63) Kim, D. H.; Rogers, J. A. Bend, Buckle, and Fold: Mechanical Engineering with Nanomembranes. *ACS Nano* **2009**, *3*, 498–501.

(64) Sun, Z.; Liao, T.; Dou, Y.; Hwang, S. M.; Park, M.-S.; Jiang, L.; Kim, J. H.; Dou, S. X. Generalized Self-Assembly of Scalable Two-Dimensional Transition Metal Oxide Nanosheets. *Nat. Commun.* **2014**, *5*, 3813.

(65) Zhou, X. F.; Tian, Z. A.; Kim, H. J.; Wang, Y.; Xu, B. R.; Pan, R. B.; Chang, Y. J.; Di, Z. F.; Zhou, P.; Mei, Y. F. Rolling up MoSe<sub>2</sub> Nanomembranes as a Sensitive Floating Photodetector. *Small* **2019**, *15*, 1902528.

(66) Zhang, B. R.; Huang, G. S.; Wang, L.; Wang, T. B.; Liu, L.; Di, Z. F.; Liu, X. Y.; Mei, Y. F. Rolled-Up Monolayer Graphene Tubular Micromotors: Enhanced Performance and Antibacterial Property. *Chem. - Asian J.* **2019**, *14*, 2479–2484.

(67) Chen, J.; Ban, D. Y.; Helander, M. G.; Lu, Z. H.; Poole, P. Near-Infrared Inorganic/Organic Optical Upconverter with an External Power Efficiency of > 100%. *Adv. Mater.* **2010**, *22*, 4900–4904.

(68) Mei, Y. F.; Huang, G. S.; Solovev, A. A.; Urenã, E. B.; Mönch, I.; Ding, F.; Reindl, T.; Fu, R. K. Y.; Chu, P. K.; Schmidt, O. G. Versatile Approach for Integrative and Functionalized Tubes by Strain Engineering of Nanomembranes on Polymers. *Adv. Mater.* **2008**, *20*, 4085–4090.

(69) Edy, R.; Zhao, Y. T.; Huang, G. S.; Shi, J. J.; Zhang, J.; Solovev, A. A.; Mei, Y. F. TiO<sub>2</sub> Nanosheets Synthesized by Atomic Layer Deposition for Photocatalysis. *Prog. Nat. Sci.* **2016**, *26*, 493–497.

(70) Wang, X. C.; Chang, J.; Wu, C. T. Bioactive Inorganic/Organic Nanocomposition for Wound Healing. *Appl. Mater. Today* **2018**, *11*, 308–319.

(71) Neumeier, B. L.; Khorenko, M.; Alves, F.; Goldmann, O.; Napp, J.; Schepers, U.; Reichardt, H. M.; Feldmann, C. Fluorescent Inorganic-Organic Hybrid Nanoparticles. *ChemNanoMat* **2019**, *5*, 24–45.

(72) Park, B.-W.; Seok, S. I. Intrinsic Instability of Inorganic-Organic Hybrid Halide Perovskite Materials. *Adv. Mater.* **2019**, *31*, 1805337.

(73) Pan, S. Q.; Zhao, Y. T.; Huang, G. S.; Wang, J.; Baunack, S.; Gemming, T.; Li, M. L.; Zheng, L. R.; Schmidt, O. G.; Mei, Y. F. Highly Photocatalytic TiO<sub>2</sub> Interconnected Porous Powder Fabricated by Sponge-Templated Atomic Layer Deposition. *Nanotechnology* **2015**, *26*, 364001.

- (74) Zhao, Y. T.; Huang, G. S.; Li, Y. L.; Edy, R.; Gao, P. B.; Tang, H.; Bao, Z. H.; Mei, Y. F. Three-Dimensional Carbon/ZnO Nanomembrane Foam as An Anode for Lithium-Ion Battery with Longlife and High Areal Capacity. *J. Mater. Chem. A* **2018**, *6*, 7227–7235.
- (75) Edy, R.; Huang, G. S.; Zhao, Y. T.; Zhang, J.; Mei, Y. F.; Shi, J. J. Atomic Layer Deposition of TiO<sub>2</sub>-Nanomembrane-Based Photocatalysts with Enhanced Performance. *AIP Adv.* **2016**, *6*, 115113.
- (76) Zhao, Y. T.; Huang, G. S.; Wang, D. R.; Ma, Y.; Fan, Z. Y.; Bao, Z. H.; Mei, Y. F. Sandwiched Porous C/ZnO/Porous C Nanosheet Battery Anodes with A Stable Solid-Electrolyte Interphase for Fast and Long Cycling. *J. Mater. Chem. A* **2018**, *6*, 22870.
- (77) Naem, F.; Naem, S.; Zhao, Y. T.; Wang, D. R.; Zhang, J.; Mei, Y. F.; Huang, G. S. TiO<sub>2</sub> Nanomembranes Fabricated by Atomic Layer Deposition for Supercapacitor Electrode with Enhanced Capacitance. *Nanoscale Res. Lett.* **2019**, *14*, 92.
- (78) Guo, Q. L.; Zhao, Y. T.; Wang, G.; Chen, D.; Zhao, H. N.; Jiang, C. M.; Huang, G. S.; Di, Z. F.; Mei, Y. F. Sponge-Templated Production Of Ultrathin ZnO Nanosheets for Printed Ultraviolet Photodetectors. *Appl. Phys. Lett.* **2019**, *115*, 122106.
- (79) Li, Y.; Zhao, Y.; Huang, G.; Xu, B.; Wang, B.; Pan, R.; Men, C.; Mei, Y. ZnO Nanomembrane/Expanded Graphite Composite Synthesized by Atomic Layer Deposition as Binder-Free Anode for Lithium Ion Batteries. *ACS Appl. Mater. Interfaces* **2017**, *9*, 38522–38529.
- (80) Wang, D.; Li, Y.; Zhao, Y.; Guo, Q.; Yang, S.; Ding, G.; Mei, Y.; Huang, G. Cycling-Induced Capacity Increase of Graphene Aerogel/ZnO Nanomembrane Composite Anode Fabricated by Atomic Layer Deposition. *Nanoscale Res. Lett.* **2019**, *14*, 69.
- (81) Jung, H.; Park, J.; Oh, I.; Choi, T.; Lee, S.; Hong, J.; Lee, T.; Kim, S.; Kim, H. Fabrication of Transferable Al<sub>2</sub>O<sub>3</sub> Nanosheet by Atomic Layer Deposition for Graphene FET. *ACS Appl. Mater. Interfaces* **2014**, *6*, 2764–2769.
- (82) Karg, M.; Lokare, K. S.; Limberg, C.; Clavel, G.; Pinna, N. Atomic Layer Deposition of Silica on Carbon Nanotube. *Chem. Mater.* **2017**, *29*, 4920–4931.
- (83) Min, Y.; Bae, E. U.; Jeong, K. S.; Cho, Y. J.; Lee, J. H.; Choi, W. B.; Park, G. S. Ruthenium Oxide Nanotube Arrays Fabricated by Atomic Layer Deposition Using A Carbon Nanotube Template. *Adv. Mater.* **2003**, *15*, 1019–1022.
- (84) Zhang, J. K.; Yu, Z. B.; Gao, Z.; Ge, H. B.; Zhao, S. C.; Chen, C. Q.; Chen, S.; Tong, X. L.; Wang, M. H.; Zheng, Z. F.; Qin, Y. Porous TiO<sub>2</sub> Nanotubes with Spatially Separated Platinum and CoOx Cocatalysts Produced by Atomic Layer Deposition for Photocatalytic Hydrogen Production. *Angew. Chem., Int. Ed.* **2017**, *56*, 816–820.
- (85) López De Dicastillo, C.; Patiño, C.; Galotto, M. J.; Palma, J. L.; Alburquerque, D.; Escrig, J. Novel Antimicrobial Titanium Dioxide Nanotubes Obtained Through A Combination of Atomic Layer Deposition and Electrospinning Technologies. *Nanomaterials* **2018**, *8*, 128.
- (86) Wang, C.-C.; Kei, C.-C.; Yu, Y.-W.; Perng, T.-P. Organic Nanowire-Templated Fabrication of Alumina Nanotubes by Atomic Layer Deposition. *Nano Lett.* **2007**, *7*, 1566–1569.
- (87) Weber, M.; Iatsunskyi, I.; Coy, E.; Miele, P.; Cornu, D.; Bechelany, M. Novel and Facile Route for The Synthesis of Tunable Boron Nitride Nanotubes Combining Atomic Layer Deposition and Annealing Processes for Water Purification. *Adv. Mater. Interfaces* **2018**, *5*, 1800056.
- (88) Hu, L.; Qi, W.; Li, Y. Coating strategies for Atomic Layer Deposition. *Nanotechnol. Rev.* **2017**, *6*, 527–547.
- (89) Sagar, L. K.; Walravens, W.; Maes, J.; Geiregat, P.; Hens, Z. HgSe/CdE (E= S, Se) Core/Shell Nanocrystals by Colloidal Atomic Layer Deposition. *J. Phys. Chem. C* **2017**, *121*, 13816–13822.
- (90) Bachmann, J.; Jing, J.; Knez, M.; Barth, K.; Shen, H.; Mathur, S.; Gösele, U.; Nielsch, K. Ordered Iron Oxide Nanotube Arrays of Controlled Geometry and Tunable Magnetism by Atomic Layer Deposition. *J. Am. Chem. Soc.* **2007**, *129*, 9554–9555.
- (91) Gu, D. F.; Baumgart, H.; Abdel-Fattah, T. M.; Namkoong, G. Synthesis of Nested Coaxial Multiple-Walled Nanotubes by Atomic Layer Deposition. *ACS Nano* **2010**, *4*, 753–758.
- (92) Jin Fan, H.; Knez, M.; Scholz, R.; Nielsch, K.; Pippel, E.; Hesse, D.; Zacharias, M.; Gösele, U. Monocrystalline Spinel Nanotube Fabrication Based on The Kirkendall Effect. *Nat. Mater.* **2006**, *5*, 627–631.
- (93) Fan, H.; Knez, M.; Scholz, R.; Nielsch, K.; Pippel, E.; Hesse, D.; Gösele, U.; Zacharias, M. Single-Crystalline MgAl<sub>2</sub>O<sub>4</sub> Spinel Nanotubes Using A Reactive and Removable MgO Nanowire Template. *Nanotechnology* **2006**, *17*, 5157.
- (94) Ku, S.; Jo, G.; Bak, C.; Kim, S.; Shin, Y.; Kim, K.; Kwon, S.; Kim, J. Highly Ordered Freestanding Titanium Oxide Nanotube Arrays Using Si-Containing Block Copolymer Lithography and Atomic Layer Deposition. *Nanotechnology* **2013**, *24*, No. 085301.
- (95) Li, J. X.; Liu, W. J.; Wang, J. Y.; Rozen, I.; He, S.; Chen, C. R.; Kim, H. G.; Lee, H. J.; Lee, H. B. R.; Kwon, S. H.; Li, T. L.; Li, L. Q.; Wang, J.; Mei, Y. F. Nanoconfined Atomic Layer Deposition of TiO<sub>2</sub>/Pt Nanotubes: Toward Ultrasmall Highly Efficient Catalytic Nanotockets. *Adv. Funct. Mater.* **2017**, *27*, 1700598.
- (96) Tan, C. L.; Cao, X. H.; Wu, X. J.; He, Q. Y.; Yang, J.; Zhang, X.; Chen, J. Z.; Zhao, W.; Han, S. K.; Nam, G. H.; Sindoro, M.; Zhang, H. Recent Advanced in Ultrathin Two-Dimensional Nanomaterials. *Chem. Rev.* **2017**, *117*, 6225.
- (97) Pi, L. J.; Li, L.; Liu, K. L.; Zhang, Q. F.; Li, H. Q.; Zhai, T. Y. Recent Progress on 2D Nobel-Transition-Metal Dichalcogenides. *Adv. Funct. Mater.* **2019**, *29*, 1904932.
- (98) Zhang, Z. P.; Yang, P. F.; Hong, M.; Jiang, S. L.; Zhao, G. C.; Shi, J. P.; Xie, Q.; Zhang, Y. F. Recent Progress in the Controlled Synthesis of 2D Metallic Transition Metal Dichalcogenides. *Nanotechnology* **2019**, *30*, 182002.
- (99) Cai, Z. Y.; Liu, B. L.; Zou, X. L.; Cheng, H. M. Chemical Vapor Deposition Growth and Applications of Two-Dimensional Materials and Their Heterostructures. *Chem. Rev.* **2018**, *118*, 6091.
- (100) Park, G. H.; Nielsch, K.; Thomas, A. 2D Transition Metal Dichalcogenide Thin Films Obtained by Chemical Gas Phase Deposition Techniques. *Adv. Mater. Interfaces* **2019**, *6*, 1800688.
- (101) Hao, W.; Marichy, C.; Journet, C. Atomic Layer Deposition of Stable 2D Materials. *2D Mater.* **2019**, *6*, 012001.
- (102) Jurca, T.; Moody, M. J.; Henning, A.; Emery, J. D.; Wang, B. H.; Tan, J. M.; Lohr, T. L.; Lauhon, L. J.; Marks, T. J. Low-Temperature Atomic Layer Deposition of MoS<sub>2</sub> Films. *Angew. Chem., Int. Ed.* **2017**, *56*, 4991.
- (103) Mughal, A. J.; Walter, T. N.; Cooley, K. A.; Bertuch, A.; Mohny, S. E. Effect of Substrate on The Growth and Properties Of MoS<sub>2</sub> Thin Films Grown by Plasma-enhanced Atomic Layer Deposition. *J. Vac. Sci. Technol., A* **2019**, *37*, No. 010907.
- (104) Kalanyan, B.; Beams, R.; Katz, M. B.; Davydov, A. V.; Maslar, J. E.; Kanjolia, R. K. MoS<sub>2</sub> Thin Films From A (Ntbu)<sub>2</sub>(NMe<sub>2</sub>)<sub>2</sub>Mo and 1-Propanethiol Atomic Layer Deposition Process. *J. Vac. Sci. Technol., A* **2019**, *37*, No. 010901.
- (105) Manzeli, S.; Ovchinnikov, D.; Pasquier, D.; Zazyev, O. V.; Kis, A. 2D Transition Metal Dichalcogenides. *Nat. Rev. Mater.* **2017**, *2*, 17033.
- (106) Dai, T. J.; Fan, X. D.; Ren, Y. X.; Hou, S.; Zhang, Y. Y.; Qian, L. X.; Li, Y. R.; Liu, X. Z. Layer-Controlled Synthesis of Wafer-Scale MoSe<sub>2</sub> Nanosheets for Photodetector Arrays. *J. Mater. Sci.* **2018**, *53*, 8436–8444.
- (107) Song, J. G.; Park, J.; Lee, W.; Choi, T.; Jung, H.; Lee, C. W.; Hwang, S. H.; Myoung, J. M.; Jung, J. H.; Kim, S. H.; Lansalot-Matras, C. L.; Kim, H. Layer-Controlled, Wafer-Scale, and Conformal Synthesis of Tungsten Disulfide Nanosheets Using Atomic Layer Deposition. *ACS Nano* **2013**, *7*, 11333–11340.
- (108) Keller, B. D.; Bertuch, A.; Provine, J.; Sundaram, G.; Ferralis, N.; Grossman, J. C. Process Control of Atomic Layer Deposition Molybdenum Oxide Nucleation and Sulfidation to Large-Area MoS<sub>2</sub> Monolayers. *Chem. Mater.* **2017**, *29*, 2024–2032.
- (109) Wang, H.; Lu, Z.; Xu, S.; Kong, D.; Cha, J. J.; Zheng, G.; Hsu, P. C.; Yan, K.; Bradshaw, D.; Prinz, F. B.; Cui, Y. Electrochemical

Tuning of Vertically Aligned MoS<sub>2</sub> Nanofilms and Its Application in Improving Hydrogen Evolution Reaction. *Proc. Natl. Acad. Sci. U. S. A.* **2013**, *110*, 19701–19706.

(110) Martella, C.; Melloni, P.; Cinquanta, E.; Cianci, E.; Alia, M.; Longo, M.; Lamperti, A.; Vangelista, S.; Fanciulli, M.; Molle, A. Engineering the Growth of MoS<sub>2</sub> via Atomic Layer Deposition of Molybdenum Oxide Film Precursor. *Adv. Electron. Mater.* **2016**, *2*, 1600330.

(111) Liu, H. F.; Antwi, K. K. A.; Wang, Y. D.; Ong, L. T.; Chua, S. J.; Chi, D. Z. Atomic Layer Deposition of Crystalline Bi<sub>2</sub>O<sub>3</sub> Thin Films and Their Conversion into Bi<sub>2</sub>S<sub>3</sub> by Thermal Vapor Sulfurization. *RSC Adv.* **2014**, *4*, 58724–58731.

(112) Dai, T. J.; Fan, X. D.; Ren, Y. X.; Hou, S.; Zhang, Y. Y.; Qian, L. X.; Li, Y. R.; Liu, X. Z. Layer-Controlled Synthesis of Wafer-Scale MoSe<sub>2</sub> Nanosheets for Photodetector Arrays. *J. Mater. Sci.* **2018**, *53*, 8436–8444.

(113) Song, J.-G.; Ryu, G. H.; Lee, S. J.; Sim, S.; Lee, C. W.; Choi, T.; Jung, H.; Kim, Y.; Lee, Z.; Myoung, J.-M.; Dussarrat, C.; Lansalot-Matras, C.; Park, J.; Choi, H.; Kim, H. Controllable Synthesis of Molybdenum Tungsten Disulfide Alloy for Vertically Composition-Controlled Multilayer. *Nat. Commun.* **2015**, *6*, 7817.

(114) Zhan, Y.; Liu, Z.; Najmaei, S.; Ajayan, P. M.; Lou, J. Large-Area Vapor-Phase Growth and Characterization of MoS<sub>2</sub> Atomic Layers on a SiO<sub>2</sub> Substrate. *Small* **2012**, *8*, 966–971.

(115) Zumeta-Dube, I.; Ortiz-Quinonez, J.-L.; Diaz, D.; Trallero-Giner, C.; Ruiz-Ruiz, V.-F. First Order Raman Scattering in Bulk Bi<sub>2</sub>S<sub>3</sub> and Quantum Dots: Reconsidering Controversial Interpretations. *J. Phys. Chem. C* **2014**, *118* (51), 30244–30252.

(116) Kastl, C.; Chen, C.; Kuykendall, T.; Shevitski, B.; Darlington, T.; Borys, N.; Krayev, A.; Schuck, P.; Aloni, S.; Schwartzberg, A. The Important Role of Water in Growth of Monolayer Transition Metal Dichalcogenides. *2D Mater.* **2017**, *4*, No. 021024.

(117) Romanov, R. I.; Kozodaev, M. G.; Myakota, D. I.; Chernikova, A. G.; Novikov, S. M.; Volkov, V. S.; Slavich, A. S.; Zarubin, S. S.; Chizhov, P. S.; Khakimov, R. R.; Chouprik, A. A.; Hwang, C. S.; Markeev, A. M. Synthesis of Large Area Two-Dimensional MoS<sub>2</sub> Films by Sulfurization of Atomic Layer Deposited MoO<sub>3</sub> Thin Film for Nanoelectronic Applications. *ACS Appl. Nano Mater.* **2019**, *2*, 7521–7531.

(118) Zeng, W.; Feng, L.; Su, J.; Pan, H.; Liu, Z. Layer-controlled and Atomically Thin WS<sub>2</sub> Films Prepared by Sulfurization of Atomic-layer-deposited WO<sub>3</sub> Films. *J. Alloys Compd.* **2018**, *745*, 834–839.

(119) Ko, K. Y.; Song, J. G.; Kim, Y.; Choi, T.; Shin, S.; Lee, C. W.; Lee, K.; Koo, J.; Lee, H.; Kim, J.; Lee, T.; Park, J.; Kim, H. Improvement of Gas-Sensing Performance of Large-Area Tungsten Disulfide Nanosheets by Surface Functionalization. *ACS Nano* **2016**, *10*, 9287–9296.

(120) Late, D. D. J.; Huang, Y. Y.-K.; Liu, B.; Acharya, J.; Shirodkar, S. N.; Luo, J.; Yan, A.; Charles, D.; Waghmare, U. V.; Dravid, V. P.; Rao, C. N. R. Sensing Behavior of Atomically Thin-Layered MoS<sub>2</sub> Transistors. *ACS Nano* **2013**, *7*, 4879–4891.

(121) Yaghi, O. M.; Li, G. M.; Li, H. L. Selective Binding and Removal of Guests in a Microporous Metal-Organic Framework. *Nature* **1995**, *378*, 703–705.

(122) Huang, X. C.; Lin, Y. Y.; Zhang, J. P.; Chen, X. M. Ligand-Directed Strategy for Zeolite-Type Metal-Organic Frameworks: Zinc(II) Imidazolates with Unusual Zeolitic Topologies. *Angew. Chem., Int. Ed.* **2006**, *45*, 1557–1559.

(123) Park, K. S.; Ni, Z.; Côté, P. A.; Choi, J. Y.; Huang, R.; Uribe-Romo, J. F.; Chae, H. K.; O'Keeff, M.; Yaghi, O. M. Exceptional Chemical and Thermal Stability of Zeolitic Imidazolate Frameworks. *Proc. Natl. Acad. Sci. U. S. A.* **2006**, *103*, 10186–10191.

(124) James, L. S. Metal-Organic Frameworks. *Chem. Soc. Rev.* **2003**, *32*, 276–288.

(125) Zhang, Z. W.; Deng, L. J.; Zhao, Z.; Zhao, Y. T.; Yang, J. Y.; Jiang, J.; Huang, G. S.; Mei, Y. F. Nickel Nanograins Anchored on a Carbon Framework for an Efficient Hydrogen Evolution Electrocatalyst and a Flexible Electrode. *J. Mater. Chem. A* **2020**, *8*, 3499–3508.

(126) Pan, Y.; Sun, K.; Liu, S.; Cao, X.; Wu, K.; Cheong, W. C.; Chen, Z.; Wang, Y.; Li, Y.; Liu, Y. Q.; Wang, D. S.; Peng, Q.; Chen, C.; Li, Y. D. Core-Shell ZIF-8@ZIF-67-Derived CoP Nanoparticle-Embedded N-Doped Carbon Nanotube Hollow Polyhedron for Efficient Overall Water Splitting. *J. Am. Chem. Soc.* **2018**, *140*, 2610–2618.

(127) Zhu, B.; Zou, R.; Xu, Q. Metal-Organic Framework Based Catalysts for Hydrogen Evolution. *Adv. Energy Mater.* **2018**, *8*, 1801193.

(128) Lu, W.; Wei, Z.; Gu, Z.; Liu, T. F.; Park, J.; Tian, J.; Zhang, M.; Zhang, Q.; Gentle, T.; Bosch, M.; Zhou, H. C.; Park, J. Tuning the Structure and Function of Metal-Organic Frameworks via Linker Design. *Chem. Soc. Rev.* **2014**, *43*, 5561–5593.

(129) Schoedel, A.; Li, M.; Li, D.; O'Keeffe, M.; Yaghi, O. M. Structures of Metal-Organic Frameworks with Rod Secondary Building Units. *Chem. Rev.* **2016**, *116* (19), 12466–12535.

(130) Xu, G.; Nie, P.; Dou, H.; Ding, B.; Li, L.; Zhang, X. Exploring Metal Organic Frameworks for Energy Storage in Batteries and Supercapacitors. *Mater. Today* **2017**, *20*, 191–209.

(131) Zheng, Y.; Zheng, S.; Xue, H.; Pang, H. Metal-Organic Frameworks for Lithium-Sulfur Batteries. *J. Mater. Chem. A* **2019**, *7*, 3469–3491.

(132) Li, S.; Xu, Q. Metal-Organic Frameworks as Platforms for Clean Energy. *Energy Environ. Sci.* **2013**, *6*, 1656–1683.

(133) Zhao, R.; Wu, Y.; Liang, Z.; Gao, L.; Xia, W.; Zhao, Y. S.; Zou, R. Metal-Organic Frameworks for Solid-State Electrolytes. *Energy Environ. Sci.* **2020**, *13*, 2386.

(134) Hou, C. C.; Wang, H. F.; Li, C.; Xu, Q. From Metal-Organic Frameworks to Single/Dual-Atom and Cluster Metal Catalysts for Energy Applications. *Energy Environ. Sci.* **2020**, *13*, 1658–1693.

(135) Li, L.; Lin, R.; Krishna, R.; Li, H.; Xiang, S.; Wu, H.; Li, J.; Zhou, W.; Chen, B. Ethane/Ethylene Separation in a Metal-Organic Framework with Iron-Peroxo Sites. *Science* **2018**, *362*, 443–446.

(136) Cui, X.; Chen, K.; Xing, H.; Yang, Q.; Krishna, R.; Bao, Z.; Wu, H.; Zhou, W.; Dong, X.; Han, Y.; Li, B.; Ren, Q.; Zaworotko, J. M.; Chen, B. Pore Chemistry and Size Control in Hybrid Porous Materials for Acetylene Capture from Ethylene. *Science* **2016**, *353*, 141–144.

(137) Cadiau, A.; Adil, K.; Bhatt, P. M.; Belmabkhout, Y.; Eddaoudi, M. A Metal-Organic Framework-Based Splitter for Separating Propylene From propane. *Science* **2016**, *353*, 137–140.

(138) McKinlay, C. A.; Morris, E. R.; Horcajada, P.; Ferey, G.; Gref, R.; Couvreur, P.; Serre, C. BioMOFs: Metal-Organic Frameworks for Biological and Medical Applications. *Angew. Chem., Int. Ed.* **2010**, *49*, 6260–6266.

(139) Du, L.; Chen, W.; Zhu, P.; Tian, Y.; Chen, Y.; Wu, C. Applications of Functional Metal-Organic Frameworks in Biosensors. *Biotechnol. J.* **2020**, 1900424.

(140) Butler, S. K.; Pearce, C.; Nail, E.; Vincent, G.; Sava Gallis, F. D. Antibody Targeted Metal-Organic Frameworks for Bio-Imaging Applications. *ACS Appl. Mater. Interfaces* **2020**, *12*, 31217.

(141) Sun, H.; Li, Y.; Yu, S.; Liu, J. Metal-organic frameworks (MOFs) for Biopreservation: From Biomacromolecules, Living Organisms to Biological Devices. *Nano Today* **2020**, *35*, 100985.

(142) Wu, J.; Chen, J.; Wang, C.; Zhou, Y.; Ba, K.; Xu, H.; Bao, W.; Xu, X.; Carlsson, A.; Lazar, S.; Meingast, A.; Sun, Z.; Deng, H. Metal-Organic Framework for Transparent Electronics. *Adv. Sci.* **2020**, *7*, 1903003.

(143) Carrasco, S. Metal-Organic Frameworks for the Development of Biosensors: A Current Overview. *Biosensors* **2018**, *8*, 92.

(144) Chang, J.; Wang, X.; Wang, J.; Li, H.; Li, F. Nucleic Acid-Functionalized Metal-Organic Framework-Based Homogeneous Electrochemical Biosensor for Simultaneous Detection of Multiple Tumor Biomarkers. *Anal. Chem.* **2019**, *91* (5), 3604–3610.

(145) Ahvenniemi, E.; Karppinen, M. Atomic/Molecular Layer Deposition: a Direct Gas-phase Route to Crystalline Metal-Organic Framework Thin Films. *Chem. Commun.* **2016**, *52*, 1139–1142.

(146) Lee, T. D.; Jamir, D. J.; Peterson, W. G.; Parsons, N. G. Protective Fabrics: Metal-Organic Framework Textiles for Rapid

Photocatalytic Sulfur Mustard Simulant Detoxification. *Matter* **2020**, *2*, 404–415.

(147) Zhao, J.; Nunn, T. W.; Lemaire, C. P.; Lin, Y.; Dickey, D. M.; Oldham, J. C.; Walls, J. H.; Peterson, W. G.; Losego, D. M.; Parsons, N. G. Facile Conversion of Hydroxy Double Salts to Metal–Organic Frameworks Using Metal Oxide Particles and Atomic Layer Deposition Thin-Film Templates. *J. Am. Chem. Soc.* **2015**, *137*, 13756–13759.

(148) Meyn, M.; Beneke, K.; Lagaly, G. Anion-Exchange Reactions of Hydroxy Double Salts. *Inorg. Chem.* **1993**, *32*, 1209–1215.

(149) Zhao, J.; Kalanyan, B.; Barton, F. H.; Sperling, A. B.; Parsons, N. G. In Situ Time-Resolved Attenuated Total Reflectance Infrared Spectroscopy for Probing Metal–Organic Framework Thin Film Growth. *Chem. Mater.* **2017**, *29*, 8804–8810.

(150) Suikkola, J.; Björminen, T.; Mosallaei, M.; Kankkunen, T.; Iso-Ketola, P.; Ukkonen, L.; Vanhala, J.; Mäntysalo, M. Screen-Printing Fabrication and Characterization of Stretchable Electronics. *Sci. Rep.* **2016**, *6*, 25784.

(151) Jeong, J.; Laiwalla, F.; Lee, J.; Ritasalo, R.; Pudas, M.; Larson, L.; Leung, V.; Nurmikko, A. Conformal Hermetic Sealing of Wireless Microelectronic Implantable Chiplets by Multilayered Atomic Layer Deposition (ALD). *Adv. Funct. Mater.* **2018**, *29*, 1806440.

(152) Ma, X.; Kumar, P.; Mittal, N.; Khlyustova, A.; Daoutidis, P.; Mkhoyan, A. K.; Tsapatsis, M. Zeolitic Imidazolate Framework Membranes Made by Ligand-Induced Permselectivation. *Science* **2018**, *361*, 1008–1011.

(153) Stassen, I.; Styles, M.; Greci, G.; Gorp, V. H.; Vanderlinden, W.; Feyter, D. S.; Falcaro, P.; Vos, D. D.; Vereecken, P.; Ameloot, R. Chemical Vapour Deposition of Zeolitic Imidazolate Framework Thin Films. *Nat. Mater.* **2016**, *15*, 304–310.

(154) Stassen, I.; De Vos, D.; Ameloot, R. Vapor-Phase Deposition and Modification of Metal–Organic Frameworks: State-of-the-Art and Future Directions. *Chem. - Eur. J.* **2016**, *22*, 14452–14460.

(155) Lausund, B. K.; Petrovic, V.; Nilsen, O. All-Gas-Phase Synthesis of Amino-Functionalized UiO-66 Thin Films. *Dalton Trans.* **2017**, *46*, 16983.

(156) Stassin, T.; Rodriguez-Hermida, S.; Schrode, B.; Cruz, A. J.; Carraro, F.; Kravchenko, D.; Creemers, V.; Stassen, I.; Hauffman, T.; De Vos, D.; Falcaro, P.; Resel, R.; Ameloot, R. Vapor-Phase Deposition of Oriented Copper Dicarboxylate Metal–Organic Framework Thin Films. *Chem. Commun.* **2019**, *55*, 10056–10059.

(157) Cruz, A. J.; Stassen, I.; Krishtab, M.; Marcoen, K.; Stassin, T.; Rodriguez-Hermida, S.; Teyssandier, J.; Pletincx, S.; Verbeke, R.; Rubio-Gimenez, V.; Tatay, S.; Marti-Gastaldo, C.; Meersschart, J.; Vereecken, P. M.; De Feyter, S.; Hauffman, T.; Ameloot, R. Integrated Cleanroom Process for the Vapor-Phase Deposition of Large-Area Zeolitic Imidazolate Framework Thin Films. *Chem. Mater.* **2019**, *31*, 9462–9471.

(158) Lausund, B. K.; Olsen, S. M.; Hansen, A. P.; Valen, H.; Nilsen, O. MOF Thin Films with Bi-Aromatic Linkers Grown by Molecular Layer Deposition. *J. Mater. Chem. A* **2020**, *8*, 2539–2548.

(159) Lee, D.; Jamir, D. J.; Peterson, W. G.; Parsons, N. G. Water-Stable Chemical-Protective Textiles via Euhedral Surface-Oriented 2D Cu–TCPP Metal–Organic Frameworks. *Small* **2019**, *15*, 1805133.

(160) Lee, T. D.; Zhao, J.; Oldham, J. C.; Peterson, W. G.; Parsons, N. G. UiO-66-NH<sub>2</sub> Metal–Organic Framework (MOF) Nucleation on TiO<sub>2</sub>, ZnO, and Al<sub>2</sub>O<sub>3</sub> Atomic Layer Deposition-Treated Polymer Fibers: Role of Metal Oxide on MOF Growth and Catalytic Hydrolysis of Chemical Warfare Agent Simulants. *ACS Appl. Mater. Interfaces* **2017**, *9*, 44847–44855.

(161) Zhao, Z.; Zhang, Z. W.; Zhao, Y. T.; Liu, J.; Liu, C.; Wang, Z.; Zheng, G. F.; Huang, G. S.; Mei, Y. F. Atomic Layer Deposition Inducing Integration of Co, N Codoped Carbon Sphere on 3D Foam with Hierarchically Porous Structures for Flexible Hydrogen Producing Device. *Adv. Funct. Mater.* **2019**, *29*, 1906365.

(162) Zhao, Z.; Kong, Y.; Liu, C.; Liu, J.; Wang, Z.; Zheng, G.; Huang, G. S.; Mei, Y. F. Atomic Layer Deposition-Induced Integration of N-Doped Carbon Particles on Carbon Foam for Flexible Supercapacitor. *J. Mater. Chem.* **2020**, *6*, 209–215.

(163) Meng, J.; Niu, C.; Xu, L.; Li, J.; Liu, X.; Wang, X.; Wu, Y.; Xu, X.; Chen, W.; Li, Q.; Zhu, Z.; Zhao, D.; Mai, L. General Oriented Formation of Carbon Nanotubes from Metal–Organic Frameworks. *J. Am. Chem. Soc.* **2017**, *139*, 8212–8221.

(164) Zhou, H. C.; Long, R. J.; Yaghi, O. M. Introduction to Metal–Organic Frameworks. *Chem. Rev.* **2012**, *112*, 673–674.

(165) Zhao, J.; Losego, D. M.; Lemaire, C. P.; Williams, S. P.; Gong, B.; Atanasov, E. S.; Blevins, M. T.; Oldham, J. C.; Walls, J. H.; Shepherd, D. S.; Browe, A. M.; Peterson, W. G.; Parsons, N. G. Highly Adsorptive, MOF-Functionalized Nonwoven Fiber Mats for Hazardous Gas Capture Enabled by Atomic Layer Deposition. *Adv. Mater. Interfaces* **2014**, *1*, 1400040.

(166) Bechelany, M.; Drobek, M.; Vallicari, C.; Abou Chaaya, A.; Julbe, A.; Miele, P. Highly Crystalline MOF-Based Materials Grown on Electrospun Nanofibers. *Nanoscale* **2015**, *7*, 5794–5802.

(167) Zhao, J.; Kalanyan, B.; Barton, F. H.; Sperling, A. B.; Parsons, N. G. In Situ Time-Resolved Attenuated Total Reflectance Infrared Spectroscopy for Probing Metal–Organic Framework Thin Film Growth. *Chem. Mater.* **2017**, *29*, 8804–8810.

(168) Dwyer, B. D.; Lee, T. D.; Boyer, S.; Bernier, E. W.; Parsons, N. G.; Jones, E. W., Jr Toxic Organophosphate Hydrolysis Using Nanofiber-Templated UiO-66-NH<sub>2</sub> Metal–Organic Framework Polycrystalline Cylinders. *ACS Appl. Mater. Interfaces* **2018**, *10*, 25794–25803.

(169) Zhao, J.; Gong, B.; Nunn, T. W.; Lemaire, C. P.; Stevens, C. E.; Sidi, I. F.; Williams, S. P.; Oldham, J. C.; Walls, J. H.; Shepherd, D. S.; Browe, A. M.; Peterson, W. G.; Losego, D. M.; Parsons, N. G. Conformal and Highly Adsorptive Metal–Organic Framework Thin Films Via Layer-by-layer Growth on ALD-Coated Fiber Mats. *J. Mater. Chem. A* **2015**, *3*, 1458–1464.

(170) Zhao, J.; Lee, T. D.; Yaga, W. R.; Hall, G. M.; Barton, F. H.; Woodward, R. I.; Oldham, J. C.; Walls, J. H.; Peterson, W. G.; Parsons, N. G. Ultra-Fast Degradation of Chemical Warfare Agents Using MOF–Nanofiber Kebabs. *Angew. Chem., Int. Ed.* **2016**, *55*, 13224–13228.

(171) Lee, T. D.; Jamir, D. J.; Peterson, W. G.; Parsons, N. G. Protective Fabrics: Metal–Organic Framework Textiles for Rapid Photocatalytic Sulfur Mustard Simulant Detoxification. *Matter* **2020**, *2*, 404–415.

(172) Stassin, T.; Stassen, I.; Marreiros, J.; Cruz, A. J.; Verbeke, R.; Tu, M.; Reinsch, H.; Dickmann, M.; Egger, W.; Vankelecom, I. F. J.; De Vos, D. E.; Ameloot, R. Solvent-Free Powder Synthesis and MOF-CVD Thin Films of the Large-Pore Metal–Organic Framework MAF-6. *Chem. Mater.* **2020**, *32*, 1784–1793.

(173) Lan, H.; Salmi, D. L.; Ronkko, T.; Parshintsev, J.; Jussila, M.; Hartonen, K.; Kemell, M.; Riekkola, M. L. Integrated Atomic Layer Deposition and Chemical Vapor Reaction for the Preparation of Metal Organic Framework Coatings for Solid-Phase Microextraction Arrow. *Anal. Chim. Acta* **2018**, *1024*, 93–100.

(174) Lausund, B. K.; Nilsen, O. All-Gas-Phase Synthesis of UiO-66 Through Modulated Atomic Layer Deposition. *Nat. Commun.* **2016**, *7*, 13578.

(175) Cruz, A. J.; Stassen, I.; Krishtab, M.; Marcoen, K.; Stassin, T.; Rodriguez-Hermida, S.; Teyssandier, J.; Pletincx, S.; Verbeke, R.; Rubio-Gimenez, V.; Tatay, S.; Marti-Gastaldo, C.; Meersschart, J.; Vereecken, P. M.; De Feyter, S.; Hauffman, T.; Ameloot, R. Integrated Cleanroom Process for the Vapor-Phase Deposition of Large-Area Zeolitic Imidazolate Framework Thin Films. *Chem. Mater.* **2019**, *31*, 9462–9471.

(176) Stassin, T.; Stassen, I.; Wauteraerts, N.; Cruz, A. J.; Kruter, M.; Coclite, A. M.; De Vos, D.; Ameloot, R. Solvent-Free Powder Synthesis and Thin Film Chemical Vapor Deposition of a Zinc Bipyridyl-Triazololate Framework. *Eur. J. Inorg. Chem.* **2020**, *2020*, 71–74.

(177) Stavila, V.; Talin, A. A.; Allendorf, D. M. MOF-Based Electronic and Opto-Electronic Devices. *Chem. Soc. Rev.* **2014**, *43*, 5994–6010.

(178) Allendorf, D. M.; Schwartzberg, A.; Stavila, V.; Talin, A. A. Roadmap to Implementing Metal–Organic Frameworks in Electronic

Devices: Challenges and Critical Directions. *Chem. - Eur. J.* **2011**, *17*, 11372–11388.

(179) Stassen, I.; Burtch, N.; Talin, A.; Falcaro, P.; Allendorf, M.; Ameloot, R. An Updated Roadmap for the Integration of Metal–Organic Frameworks with Electronic Devices and Chemical Sensors. *Chem. Soc. Rev.* **2017**, *46*, 3185–3241.

(180) Krishtab, M.; Stassen, I.; Stassin, T.; Cruz, A. J.; Okudur, O. O.; Armini, S.; Wilson, C.; De Gendt, S.; Ameloot, R. Vapor-Deposited Zeolitic Imidazolate Frameworks as Gap-Filling Ultra-Low-K Dielectrics. *Nat. Commun.* **2019**, *10*, 3729.

(181) Lemaire, P.; Zhao, J.; Williams, P.; Walls, H.; Shepherd, S.; Losego, M.; Peterson, G.; Parsons, G. Copper Benzenetricarboxylate Metal–Organic Framework Nucleation Mechanisms on Metal Oxide Powders and Thin Films Formed by Atomic Layer Deposition. *ACS Appl. Mater. Interfaces* **2016**, *8*, 9514–9522.

(182) Lee, D.; Zhao, J.; Peterson, G.; Parsons, G. Catalytic “MOF-Cloth” Formed via Directed Supramolecular Assembly of UiO-66-NH<sub>2</sub> Crystals on Atomic Layer Deposition-Coated Textiles for Rapid Degradation of Chemical Warfare Agent Simulants. *Chem. Mater.* **2017**, *29*, 4894–4903.

(183) Barton, H.; Davis, A.; Parsons, G. The Effect of Surface Hydroxylation on MOF Formation on ALD Metal Oxides: MOF-525 on TiO<sub>2</sub>/Polypropylene for Catalytic Hydrolysis of Chemical Warfare Agent Simulants. *ACS Appl. Mater. Interfaces* **2020**, *12*, 14690–14701.